"revision 2"

Carboniferous inherited grain and age zoning of monazite and xenotime from leucogranites in far-eastern Nepal: Constraints from electron probe microanalysis

Takeshi Imayama[1,*], and Kazunori Suzuki[1]

[1]Center for Chronological Research, Nagoya University, Nagoya 464-8602, Japan

*Present address: Department of Earth and Environmental Science, Chonbuk National University, Jeonju 561-756, Republic of Korea Email:t.imayama@gmail.com

ABSTRACT

Chemical Th-U-total Pb isochron method (CHIME) of monazite and xenotime from three leucogranites in far-eastern Nepal revealed the presence of Carboniferous inherited grains of monazite and intense intrusion of leucogranites around 18-16 Ma in the High Himalaya. In garnet-bearing sillimanite-muscovite-biotite leucogranite, most monazite grains have inherited cores with the chemical dates of *c.* 504-418 Ma and *c.* 342-272 Ma, which were overgrown by Early Miocene mantles and rims of 17.9 ± 1.5 Ma. Early Ordoviciain and Carboniferous ages are rarely found in the same euhedral-subhedral cores. In addition to the previously recognized Early Paleozoic magmatism, monazite cores with Carboniferous ages in Early Miocene leucogranites provide evidence for two periods of magmatism at the base of the High Himalaya prior to the Cenozoic Himalayan orogeny. In muscovite-biotite leucogranite, no inherited domains were observed in monazite and xenotime grains. They yielded the CHIME monazite and xenotime dates of 16.1 ± 2.0 Ma and 19.8 ± 6.5 Ma respectively. Monazite grains adjacent to xenotime have significantly lower concentrations of UO_2 and Y_2O_3 compared to those isolated from xenotime. These results imply that xenotime influences Y and U contents in monazite, reflecting local equilibrium system. In aplitic

leucogranite, monazite grains yielded the mean of apparent chemical date of 18.0 ± 2.2 Ma. The CHIME monazite ages of *c.* 18-16 Ma in three leucogranites reflect the timing of melt crystallization.

Keyword: Himalayan leucogranite, Carboniferous monazite, chemical age, xenotime, age zoning

INTRODUCTION

The Himalaya orogen is a typical continent-continent collision formed by the Indian-Asian collision, and the magmatism and metamorphism mainly occurred during the Cenozoic time in response to regional crustal shortening and tectonic burial (e.g., Hodges et al. 2000). The Himalayan leucogranites are generally regarded as S-type leucogranites originating from partial melting at the base of the High Himalaya (e.g., France-Lanord and Le Fort 1988; Inger and Harris 1993; Harris and Massey 1994). Numerous radiometric-dating studies of zircon, monazite, and xenotime indicate that most leucogranites in the Himalaya were produced in Early Miocene time (e.g., Searle et al. 2003 and references therein; Viskupic et al. 2005). In eastern Nepal, U-Th-Pb monazite ages of *c.* 24 Ma and 16 Ma from leucogranite plutons have been determined using isotope dilution thermal ionization mass spectrometry (TIMS) on individual grains from heavy mineral separates (Schärer 1984; Copeland et al. 1988; Hodges et al. 1998; Simpson et al. 2000; Viskupic and Hodges 2001; Viskupic et al. 2005) or by secondary-ion mass spectrometry and laser ablation inductively coupled plasma mass spectrometry microanalyses of spots on monazite grains in thin section (Harrison et al. 1999; Murphy and Harrison 1999; Catlos et al. 2002; Streule et al. 2010; Visoná et al. 2012).

Some workers have suggested the involvement of early Palaeozoic orogenic rocks along the Indian margin of Gondwana in the Himalaya based on the U-Pb ages of inherited zircon from leucogranite (e.g., Gehrels et al. 2006; Cawood et al. 2007). In the Kathmandu area in central Nepal, Gehrels et al. (2006) reported U-Pb zircon ages of 480 ± 11 Ma and 484 ± 11 Ma for two granites and 473 ± 11 Ma and 476 ± 10 Ma for two granitic dykes. Cawood et al. (2007) also reported U-Pb zircon ages of 477 ± 4 Ma and 478 ± 17 Ma for two granites in the Kathmandu area, and detrital zircon ages, the youngest of which were *c*. 570–500Ma from two xenoliths in the same granites. These ages are assigned to a Cambro-Ordovician orogenic event that occurred during the assembly of Gondwana (Gehrels et al. 2006; Cawood et al. 2007). Ordoviciain to early Silurian magmatic ages were also recognized in the orthogneisses in the High Himalaya; they yielded U-Pb zircon ages of *c.* 475-430 Ma in far-eastern Nepal (Imayama et al. 2012) and *c.* 470–465 Ma in the Everest area in eastern Nepal (Viskupic and Hodges, 2001).

Monazite, like zircon, commonly exhibit complex internal zoning of composition and age at the micrometer scale (e.g., Williams et al. 2007). Inherited monazite has been identified in Himalayan leucogranite (Copeland et al. 1988; Harrison et al. 1995). Inherited monazite ages of 471 ± 10 Ma from the Everest leucogranites were dated by discordia of different grains using TIMS (Copeland et al. 1988). Four spots on one grain obtained via in situ analysis by ion microprobe give $^{208}Pb/^{232}Th$ ages between 614 and 574 Ma indicating the presence of inherited $^{208}Pb^*$ in monazite from the Manaslu leucogranite (Harrison et al. 1995). In situ dating methods are nondestructive and allow dates to be interpreted in textural context, and analysis of zones in the grain of interest in thin section is feasible (e.g., Harrison et al. 2002; Williams et al. 2007). The high

spatial resolution is a great advantage over single grain dating (e.g., TIMS) to differentiate between inherited, pro-, peak-, and retro-grade domains. However, despite its potential significance for understanding tectonic settings and processes prior to the Cenozoic Himalayan orogeny, the age spectrum and age zoning of inherited monazite grains in leucogranites are little reported. Hence, the application of high spatial resolution dating techniques to obtain more precise constraints on the history of complexly zoned monazite in leucogranites is required. Additionally, microanalysis of xenotime for geochemistry and geochronology is useful for understanding magmatic processes and the geochemistry of monazite (e.g., Hetherington et al. 2008).

The chemical Th-U total-Pb isochron method (CHIME) for in situ age dating using the electron probe microanalyser (EPMA) provide dates from *c.* 3-5 μm size domains in monazite (Suzuki and Adachi 1991; Suzuki and Kato 2008). Compositional mapping techniques provide a detailed insight into complex internal zoning, which may be correlated with age. Here we present compositional maps and CHIME dates for monazite and xenotime from leucogranites in the far-eastern Nepalese Himalaya. This study demonstrates the successful application of CHIME dating to Cenozoic accessory minerals that inherit Carboniferous ages in rocks from the High Himalaya. Their petrogenesis is discussed, as are their significance for the magmatic and tectonic history of the Himalayan orogeny.

GEOLOGICAL SETTING AND LEUCOGRANITE SAMPLES

The Lesser Himalayan Sequence consisting of low-grade metasediments has a thrust contact with the overlying High Himalayan Crystalline Sequence (HHCS) along the Main Central Thrust in far-eastern Nepal (Fig. 1: Schelling 1992; Goscombe et al. 2006;

Imayama et al. 2010). The HHCS is dominated by leucogranites, amphibolite to granulite facies gneisses, and migmatites, and is bounded by the extensional South Tibetan Detachment to the north. The opposing-sense movements along the Main Central Thrust and the South Tibetan Detachment are believed to have caused the southward extrusion of the HHCS within the framework of channel flow (e.g., Beaumont et al. 2004; Jamieson et al., 2004; Godin et al. 2006) and tapering wedge model (e.g., Bollinger et al., 2006; Kohn, 2009). The spectrum of detrital zircon ages for the HHCS has broad peaks at *c.* 1300–500 and *c.* 2700–2300 Ma, whereas those in the Lesser Himalayan Sequence range from *c.* 2600 to 1600 Ma with a prominent peak at *c.* 1800 Ma (e.g., DeCelles et al. 2000; Martin et al. 2005; Gehels et al. 2011). Based on the minimum age of detrital zircon from metasediments, the upper age limit of sedimentation of protoliths to the HHCS and the Lesser Himalayan Sequence are interpreted as late Proterozoic to Early Cambrian and middle Proterozoic respectively (e.g., Parish and Hodges 1996; Myrow et al. 2003). The South Tibetan Detachment separates the HHCS from the overlying Tethys Himalayan Sequence of Early Paleozoic to Early Cenozoic age (e.g., Burchifiel et al. 1992; Brookfield 1993). Leucogranite bodies occur in the HHCS, and their size ranges from a few centimeter-sized sills and dikes to several kilometer-sized plutons (e.g., Hodges 2000). Aplitic veins are seen with the leucogranites, and in far-eastern Nepal, several quartzofeldspathic veins are seen along the Main Central Thrust. However, the low-grade Lesser Himalayan Sequence rocks never show evidence of melting (Imayama et al. 2012).

In central and eastern Nepal, evidence of Early Paleozoic metamorphism is based on U-Th-Pb ages of monazite grains from high-grade metamorphic rocks (Catlos et al. 2002; Kohn et al. 2004; Gehrels et al. 2006). Monazite inclusions in garnet

porphyroblasts have been dated at 451 ± 6 Ma in the Langtang region (Kohn et al. 2004), 490 ± 24 Ma in the Kathmandu (Gehrels et al. 2006), and 436 ± 8 Ma and 548 ± 17 Ma in the Everest region (Catlos et al., 2002). Monazite from kyanite leucosome in the Annapurna yielded a U-Pb age of 460 ± 8 Ma (Godin et al. 2001). Metamorphism during the Cenozoic has been mainly recognized as intermediate P/T- type metamorphism in the Late Eocene–Oligocene (*c.* 38–32 Ma; Simpson et al. 2000; Godin et al. 2001) and high-T at medium- to low-pressure metamorphism caused the widespread anatexis in the Early–Middle Miocene at *c.* 26–18 Ma (e.g., Simpson et al. 2000; Viskupic et al. 2005). However, recent reports of Early Oligocene migmatites in the High Himalaya have indicated that Early Oligocene anatexis was more prevalent in the High Himalaya than previously thought (e.g., Groppo et al. 2010; Imayama et al. 2012).

Along the Tamor-Ghunsa section in far-eastern Nepal, metamorphic peak-T conditions increase upwards from 570 °C to 670 °C along the Main Central Thrust, through a significant temperature increase to 740 °C, and reach roughly isothermal conditions (*c.* 710–810 °C) in the middle part of HHCS (Imayama et al. 2010). Metamorphic pressure conditions at peak-T record pressures of 11 kbar at the base of the HHCS, with pressure gradient of *c.* 1.2–1.6 kbar/km across the MCT (Imayama et al., 2010). In the middle part of the HHCS, pressures apparently decrease upwards from *c.* 8–10 to 5 kbar (Imayama et al. 2010).

Based on mineral assemblages the majority of leucogranites intruding the HHCS along the Tamor-Ghunsa section may be classified into three groups: muscovite-biotite ± sillimanite; garnet-bearing sillimanite-muscovite-biotite; and, tourmaline-bearing muscovite-biotite leucogranites (Fig. 1). Most leucogranites are medium-grained with a

145 distinct foliation; a few leucogranites displays a massive coarse-grained texture.
146 Muscovite-biotite ± sillimanite leucogranites with quartz, plagioclase, K-feldspar, and
147 accessory minerals apatite, monazite, zircon, and xenotime are the most common
148 lithology. Garnet-bearing sillimanite-muscovite-biotite leucogranites also contain quartz,
149 plagioclase, and K-feldspar, with accessory apatite, monazite, and zircon. Garnet grains
150 range in size from 1 to 5 mm, and are subhedral to euhedral. They are occasionally
151 broken and partially replaced by biotite and chlorite along the fractures.
152 Tourmaline-bearing muscovite-biotite leucogranites also contain plagioclase, quartz,
153 and K-feldspar. Tourmaline forms euhedral prisms of 3 to 10 mm in length.
154 For CHIME monazite and xenotime dating, two leucogranites (L09 and L02) that
155 intruded sillimanite migmatites, and one aplitic leucogranite (L05) from the
156 middle-upper parts of the HHCS along the Tamor-Ghunsa section were studied (Fig. 1).
157 The two leucogranites were selected because they intrude migmatites with well
158 constrained P-T histories. Garnet-bearing sillimanite-muscovite-biotite leucogranite
159 (sample L09) was collected from a leucogranite dyke below the High Himal Thrust,
160 which is a large-scale brittle-ductile shear zone (Figs. 1 and 2a, Goscombe et al. 2006).
161 In sample L09, sillimanite occurs as euhedral prisms with a maximum length of 3.5 mm
162 (Fig. 2b). Garnet porphyroblasts are present in minor amounts (<5%), and are subhedral
163 to euhedral (Fig. 2b). K-feldspar predominates over plagioclase, and has occasional
164 inclusions of garnet. Peak P-T conditions for the sillimanite migmatite below the High
165 Himal Thrust are inferred to be *c.* 8-10 kbar and *c.* 760-800 ºC (Imayama et al. 2010).
166 U-Pb dates of zircon cores in the sillimanite migmatites yielded inherited ages of *c.*
167 1000 to 800 Ma. The cores are surrounded by two overgrown rims. U-Pb ages from
168 inner rims around cores are *c.* 33-28 Ma and the outer rims are *c.* 27-23 Ma. These dates

have been interpreted to be the ages of partial melting at peak temperatures and garnet breakdown during retrogression (Imayama et al. 2012). Zircon grains from another muscovite-biotite leucogranite dyke (H2708 of Imayama et al., 2012) in the sillimanite migmatites have inherited cores with ages ranging from 2840 to 370 Ma, overgrown by two textural younger zones. The inner rim was dated to 18.3 ± 0.3 Ma and is interpreted to be the time of the anatectic melting near the peak-T stage of metamorphism, while the outer rim was dated to 16.3 ± 0.2 Ma and corresponds to the time of melt crystallization.

Muscovite-biotite leucogranite (sample L02) was collected from a 4-6 m wide leucogranite sill *c.* 0.5 km east of Ghunsa in far-eastern Nepal (Figs. 1 and 2c). Sample L02 includes fibrolitic sillimanite that forms thin films along the grain boundary of quartz and plagioclase. Chlorite is present in minor amounts (<5%) and biotite also shows partial alteration to chlorite (Fig. 2d). Plagioclase occurs as inclusion-rich (inclusions of quartz and biotite) subhedral grains. The P-T conditions for the surrounding sillimanite migmatites during the peak-T stage of metamorphism are inferred to be *c.* 5-8 kbar at *c.* 770-810 ºC (Imayama et al. 2010).

Leucogranites at the highest structural level of the HHCS were dated by sampling an aplitic leucogranite (L05) collected from float at the Kanchenjunga basecamp. It is proposed that the material represents part of the plutonic rocks of the Jannu Granites (Fig. 1). Sample L05 is a fine-grained massive granite that is dominated by quartz with minor amounts of biotite, muscovite, fibrolite, and feldspars. The main accessory minerals are apatite, monazite, and zircon.

ANALYTICAL METHODS

Elemental mapping of garnet, monazite, and xenotime were carried out on thin sections of leucogranites L09, L02, and L05 using a JEOL JXCXA-733 EPMA at Nagoya University. The calculation of CHIME monazite and xenotime dates followed the procedures given in Suzuki and Kato (2008, and references therein) except for the integration time of X-ray intensities. To adapt the CHIME technique for young monazite and xenotime, X-ray intensities for each peak and each background were integrated over 800-3200 s and over 400-1600 s respectively for Th, U, Pb, and Y, and over 40 s and 20 s for all other elements. The detection limits of PbO are improved by adopting a 3200 s integration time and a 150 nA probe current, and they are *c.* 45 ppm on monazite and *c.* 55 ppm on xenotime at the 2σ confidence level. The relative error for 0.01 wt. % PbO determination is *c.* 20% for monazite and *c.* 30% for xenotime at the 1σ confidence level. To identify possibly disconcordant analyses from damaged or metamict domains, the criteria of $0.95<(Ca+Si)/(Th+U+Pb+S)<1.05$ for monazite and CaO<0.05 wt.% for xenotime were adopted (Suzuki and Kato 2008). For overcoming the problematic secondary fluorescence from adjacent K-bearing minerals during the analysis (e.g., Jercinovic and Williams 2005), xenotime and monazite grains with less than 0.02 wt. % detected K_2O were selected for calculation of the chemical age. Error on the isochron age was determined by the best-fitting regression line, taking account of uncertainties in the individual spot analyses. The results of EPMA of monazite and xenotime in leucogranites are listed in Tables 1 and 2, respectively. Further details of analytical methods are provided in the electronic depository document.

RESULTS

Garnet-bearing sillimanite-muscovite-biotite leucogranite (sample L09)

Garnet porphyroblasts have little to no compositional zoning and are usually in contact with quartz, plagioclase, and K-feldspar, and include abundant apatite and monazite inclusions (Fig. 3). Nineteen monazite [(REE,Th,Ca)(P,Si)O_4] grains ranging in size from *c.* 50 to 200 μm were analyzed, and are mostly included in plagioclase and quartz. Euhedral zircon is observed in close proximity to several monazite grains (Fig. 4a). BSE images for most monazite grains (grains 1 to 8 and 11 to 16) reveal that they have relatively darker cores (e.g., Fig. 5a-c, grain 2, 15 and 11). Yttrium, U, and Th in these grains show concentric zoning with Y-rich cores and rims, separated by a mantle with lower Y content (Fig. 5a-c). Th and U concentrations have an inverse relationship with Y content in many grains (Fig. 5a-c). In a few monazite grains (grains 9, 10 and 17 to 19), Y has a patchy distribution, with an inverse relationship to BSE intensity, and no clear core-rim texture (e.g., Fig. 5d, grain 18). The U content shows a weak inverse relationship with Y content (Fig. 5d).

Most monazite grains have CaO concentrations between 0.8 and 2.2 wt. % with a positive correlation between CaO and (ThO_2 + UO_2) (Fig. 6a). The SiO_2 content in most grains is less than 1.0 wt. % (Fig. 6b) indicating that the monazite-cheralite [Ca,Th(PO_4)$_2$] substitution ($2REE^{3+} \leftrightarrow Ca^{2+} + Th^{4+}$ or U^{4+}), rather than the monazite-huttonite ($ThSiO_4$) substitution ($P^{5+} + REE^{3+} \leftrightarrow Si^{4+} + Th^{4+}$ or U^{4+}), is dominant. Except for patchy-zoned grains (e.g. Fig. 5d), the cores generally have higher Pb abundance than the mantle and rims (Fig. 6c, Table 1). Patchy zoned grains have low measured Pb abundances, similar to those in the mantle and rims of concentrically zoned grains (Fig. 6c). Y_2O_3 and UO_2 contents in patchy- zoned grain are indistinguishable from those in the mantles and rims of zoned grains (Fig. 6d).

The PbO vs. ThO* (ThO_2* is the sum of ThO_2 and the ThO_2 equivalent of UO_2)

diagrams for analyzes of monazite cores, mantles, rims and patch-zoned grains is shown in Fig. 7. Dates for monazite cores fall into two age populations at *c.* 504-418 Ma and *c.* 342-272 Ma, and the means of apparent chemical dates are 449.0 ± 33.8 Ma (n=27, 1SD) and 320.8 ± 17.4 Ma (n=29, 1SD) respectively (Fig. 7a). Early Ordoviciain to early Silurian and Carboniferous dates are measured in euhedral to subhedral cores in different grains respectively (Fig. 5a and b). Grain 11 (Fig. 5c) represents a population with core domains with Silurian (439-418 Ma) and Carboniferous (341-312 Ma) dates respectively. These high-Y cores, similar to those in Fig. 5-c, were overgrown by Early-Middle Miocene mantles and rims ranging between 27 and 11 Ma. The patchy-zoned monazite grains similar to those in Fig. 5d also yielded apparent chemical ages of 27-11 Ma. Analysis of mantles, rims, and patchy-zoned grains yielded a mean apparent age of 18.1 ± 3.5 Ma (n=124, 1SD) and an isochron age of 17.9 ± 1.5 Ma (2σ, MSWD = 1.19) with an intercept value at the origin (Fig. 7b). These Cenozoic dates are interpreted to reflect monazite growth during the Himalayan thermal event.

Muscovite-biotite leucogranite (sample L02)

Monazite grains are euhedral to subhedral and commonly included in plagioclase, K-feldspar and quartz, and rarely biotite and garnet. Monazite grains are sometimes found in clusters with xenotime (YPO_4) (Fig. 4b). In such clusters BSE images show that monazite domains in contact with xenotime are partly altered or dissolved (Fig. 4c), and they have micro-inclusions of thorite and uraninite. Monazite grains contain inclusions of apatite, quartz, and sulfide minerals. Compositional X-ray maps for Y, U, and Th for monazite in leucogranite L02 are shown in Fig. 8. Monazite grain 2 has a high Y core and a lower Y rim (Fig. 8a). On the other hand, Th and U have an irregular

distribution with a high U and Th concentrations towards a prismatic termination. Thorium and U contents show a weak correlation with Ca content, suggesting that some charge-compensation is achieved by the monazite-cheralite substitution (Fig. 8a). In the altered domains of monazite, U content decreases markedly, compared to unaltered inclusion-free domains (Fig. 8b and c). Locations for EPMA spots avoided altered inclusion-rich domains.

Based on their compositional characteristics, monazite is grouped into two types. The first type (grains 2, 3, 5, and 6) is characterized by high concentrations of CaO (2.2-2.7 wt. %) and Y_2O_3 (3.1-4.3 wt. %) with positive correlation between CaO and $ThO_2 + UO_2$ (Fig. 9a and b). This, coupled with the low SiO_2 concentration of 0.22-0.43 wt. %, suggests that the monazite-cheralite substitution is the principal solid-solution mechanism operating in the high Ca type monazite (Fig. 9c). The second type (grains 1, 4, 7, 8 and 9) is characterized by higher concentrations of SiO_2 (1.6-2.8 wt. %) coupled with low CaO (0.2-0.4 wt. %) and Y_2O_3 (0.4-1.0 wt. %), and exhibit compositional solid-solution exchange dominated by the monazite-huttonite substitution (Fig. 9a-c). This type of monazite occurs exclusively in clusters with xenotime (Fig. 8b and c). The huttonite (SiO_2)-rich monazite grains are significantly lower in UO_2 than the cheralite (CaO)-rich monazite grains (Fig. 9c), while the ThO_2 content is similar in the both types (Table 1).

Cheralite-rich grains (grain 2, 3, 5, and 6) and huttonite-rich grains (grain 1, 4, 7, 8, and 9) yielded chemical dates of 21-16 Ma and 22-14 Ma (Table 1), with mean apparent chemical dates of 17.7 ± 1.2 Ma (n=28, 1SD) and 17.7 ± 2.3 Ma (n=16, 1SD) respectively. In these grains, there is no significant age difference between core and rim (Fig. 8). Despite the contrasting substitutions, forty four analyses on nine grains in

sample L02 show a linear distribution on the PbO-ThO* diagram (Fig. 10a). Data points from cheralite-rich grains are located at the higher ThO_2* region, owing to the high concentration of UO_2. Regression of data points yields an isochron of 16.1 ± 2.0 Ma (2σ, MSWD = 0.46) with an intercept value at the origin (Fig. 10a). This suggests there is no significant difference between the crystallization ages of the cheralite- and huttonite-rich monazite grains.

Representative xenotime grains show oscillatory zoning in BSE image (Fig. 4d). On the other hand some xenotime grains display zoning patterns with irregular brighter BSE domains surrounded by relatively darker domains (Fig. 8b). The brighter domains have slightly lower Y_2O_3 and higher UO_2 contents, compared to the darker domains (Fig. 8b). Both Y_2O_3- and UO_2-poor domains are observed as very thin rims (Fig. 8b). Except for the rim, a total of 23 spots were analyzed for CHIME xenotime dating. Between and within xenotime grains, Y_2O_3 and UO_2 contents vary from 35.5 to 39.2 wt. % and from 3.2 to 6.3 wt. %, respectively (Table 2). The mean of apparent chemical dates from xenotime grains is 18.6 ± 3.0 Ma (n=23, 1SD). The relationship between PbO and UO_2* is shown in Fig. 10b. Regression of twenty three data points yielded an isochron of 19.8 ± 6.5 Ma (2 σ , MSWD＝1.29) with an intercept value at the origin (Fig. 10b). The apparent age of xenotime is indistinguishable from the monazite dates, indicating contemporaneous crystallization of both minerals.

Aplitic leucogranite (sample L05)

The internal texture of the monazite grains is irregular, with little or no compositional zoning of Y_2O_3, UO_2, and ThO_2 (Fig. 11). The monazite grains have CaO concentrations between 0.9 and 1.5 wt. % (Fig. 12a) and low SiO_2 concentrations

between 0.2 and 0.4 wt. % (Fig. 12b), indicating that the monazite-cheralite substitution is dominant. The total concentrations of ThO_2 and UO_2 in the monazite grains (5.4 to 8.0 wt. %) are lower than those in monazite from the other two samples (Fig. 12), and the compositional range is smaller. For such homogenous compositions in monazite grains, it is hard to construct an isochron. The apparent chemical date calculated from thirty two analyzed points in three monazite grains was 18.0 ± 2.2 Ma (n=32, 1SD), which is in statistically agreement with the Cenozoic isochron age of sample L09.

DISCUSSION

Formation of Pre-Himalayan monazite

In leucogranite L09, the Y content of cores in monazite is strongly correlated with high Pb content, compared to Cenozoic monazite domains (Fig. 6c), and thus the high-Y cores are indicative of inheritance. The Ordovician to Silurian ages (*c.* 504-418 Ma) from inherited cores in this study are consistent with previously published dates of 471 ± 10 Ma for inherited monazite from leucogranites (Copeland et al. 1988) and zircon U-Pb ages of *c.* 490-430 Ma for the orthogneiss and leucogranite of the HHCS (e.g., Viskupic and Hodges 2001; Cawood et al. 2007; Gehrels et al. 2011; Imayama et al. 2012). This supports the interpretation that a regional scale pre-Himalayan early Ordovician orogenic event (possibly up to Silurian) occurred in the HHCS, which would have influenced basement architecture during Cenozoic collision (e.g., LeFort et al. 1986; DeCelles et al. 2000; Gehrels et al. 2006; Cawood et al. 2007; Gehrels et al. 2011).

In terms of the broad age spectrum of inherited ages younger than the Early Paleozoic (Fig. 7a), the interpretation is complicated by the possibility that ages resulted

337 from diffusive Pb loss and hydrothermal alteration (cf. Harrison et al. 1999; Budzyń et
338 al. 2010). However, the significant number of data points for inherited monazite
339 concentrated around the 320 Ma reference isochron in PbO vs. ThO* space suggests
340 that the dates (*c.* 342-272 Ma) have geologic significance (Fig. 7a). The Carboniferous
341 dates are significant because they may represent an additional thermal event during
342 Middle-Late Paleozoic, in addition to the early Ordovician orogenic event. Kohn et al.
343 (2004) reported one analyses of monazite in a garnet porphyroblast from a migmatite in
344 central Nepal with a Th-Pb age of 309 ± 7 Ma. The other reported occurrence of
345 Middle-Late Paleozoic granites in the High Himalaya are Early Permian alkaline
346 granitoids from the Indian Himalaya of southeast and western Zanskar, which could
347 represent the active Indian plate margin during rifting of Gondwana and associated
348 igneous activity (Spring et al. 1993; Noble et al. 2001).
349 Some researchers have suggested the existence of a passive margin setting along the
350 northern Indian margin of Gondwana from Early Paleozoic to the Cenozoic Himalayan
351 Orogeny. This is based on the stratigraphically continuous and thick Tethys Himalayan
352 Sequence of Early Paleozoic to Early Cenozoic age (e.g., Brookfield 1993). Whereas
353 the relatively coherent stratigraphy with fossiliferous sediments is found in the Tethys
354 Himalayan Sequence (Brookfield 1993, and reference there in), Middle-Late Paleozoic
355 stratigraphic unconformities between Early Ordovician and Late Carboniferous
356 sediments are observed at many places in the Lesser Himalaya in Nepal (e.g., Sakai
357 1991; Upreti 1999). The absence of younger Paleozoic deposits could be attributed to
358 uplift and erosion or non‐deposition resulting from pre-Himalayan orogenic events
359 (Brookfield, 1993; Geherls et al. 2011). In this respect, a Carboniferous orogenic event
360 at the base of the High Himalaya deserves consideration in addition to the previously

recognized Early Paleozoic orogenic event.

Based on experimental work, fluid-induced reactions are capable of completely resetting the monazite Th–Pb chronometer such that recrystallized domains accurately record the timing of the fluid-alteration (e.g., Williams et al. 2011). Thus, there may be the possibility that a few Carboniferous ages in this study could have resulted from fluid-induced alteration of the Th-U-Pb system in originally Early Paleozoic monazite domains. However, there is no age zoning such as early Ordoviciain to early Silurian cores surrounded by Carboniferous mantles, which would be likely in the case of fluid alteration. In addition, none of the cores have the patchy zoning and dominant huttonite-type substitution that is characteristic of monazite grains influence by fluid-induced alternation (Townsend et al. 2000; Williams et al. 2011). Hence, we do not favor an interpretation that requires fluid-induced alteration of Early Paleozoic monazite resulting in Carboniferous dates, although we cannot entirely rule out the possibility that fluid infiltration may have occurred in grains with cheralite substitution.

This is the first conclusive description of inherited Carboniferous monazite from garnet-bearing leucogranites in the Himalaya. Previous researchers have focused geochronological studies on two-mica and tourmaline-bearing leucogranites that are pervasive throughout the Himalaya (e.g., LeFort et al. 1986). Given that the Carboniferous monazite grains are only reported from one garnet-bearing leucogranite, additional studies are needed to confirm whether this represents a larger, regionally significant period of magmatism during Middle-Late Paleozoic.

Growth of contrasting monazite compositions and xenotime in the Cenozoic

The euhedral zircon (Fig. 4a) and oscillatory zoned xenotime (Fig. 4d) that coexist

with monazite in leucogranites are typical of mineral growth from a melt during cooling (e.g., Corfu et al. 2003). The SHRIMP age (c. 16 Ma) of the oscillatory zoned outer rim in zircon from leucogranite dyke (H2708 of Imayama et al., 2012) in far-eastern Nepal is consistent with the CHIME monazite ages of *c.* 18-16 Ma in three leucogranites in this study. This indicates that the monazite ages reflect the timing of melt crystallization and the CHIME is a useful tool for obtaining reasonable monazite ages for young (Cenozoic) monazite, in particular monazite with high actinide contents.

The patchy-zoned monazite grains in leucogranite L09 could be texturally interpreted as a retrograde, sub-solidus monazite, as suggested by Townsend et al. (2000). However, the compositional characteristics from the patchy-zoned monazite grains are indistinguishable from the other Cenozoic monazite grains (Fig. 8). The experimental results showing significant depletion in Ca, U, and Y in the altered domains (Williams et al. 2011) are in accord with the characteristics of huttonite-rich monazite grains in leucogranite L02. Microinclusion-rich domains adjacent to grain boundaries with xenotime (Fig. 8b) could provide a pathway for fluid-assisted PbO loss from the original monazite by a coupled dissolution–precipitation process (cf. Geisler et al. 2007). Hence, it may be that the formation of huttonite-rich monazite in leucogranite L02 is related to fluid alteration. On the other hand, the experiments described by Williams et al. (2011) show that distinct compositional (altered and unaltered) domains tend to retain sharp boundaries in individual grains. In this study, however, the occurrence of huttonite-rich monazite grains is spatially associated with xenotime, and the huttonite- and cheralite-rich monazite domains are not mixed in individual grains. The observation implies that the monazite was altered grain by grain or the composition of huttonite-rich monazite is controlled by the presence, or reaction with, xenotime. The

later interpretation is preferred because it is well known that the behavior of yttrium and uranium in monazite is influenced by the partitioning of these elements between monazite and xenotime (e.g., Pyle et al. 2001).

Generally, the different Y and U contents in monazite are a consequence of formation at different P-T conditions (i.e. different metamorphic/magmatic stages: e.g., Pyle and Spear 2003; Williams et al. 2007; Spear and Pyle 2010). Nevertheless, the crystallization of huttonite- and cheralite-rich monazite grains with different Y and U contents in leucogranite L02 show no obvious age difference (Fig. 10). This suggests that monazite growth occurred simultaneously and the contrasting compositions reflect not different P-T condition, but effective bulk rock composition. The interpretation is possible if the scales of chemical equilibrium of trace elements in natural magmas are limited to a local reactive subsystem, rather than total equilibrium at meso- and macro-scales (e.g., Pichavant et al. 2007). When monazite and xenotime contemporaneously crystallize from the melt, and if local equilibrium was maintained at millimeter-scale between the monazite and xenotime, the growing monazite grains had significantly lower Y_2O_3 and UO_2 as a result of the enrichment of Y and U in xenotime, compared to monazite growing in isolation from xenotime. Considering that the occurrence of huttonite-rich monazite grains in thin section is spatially associated with xenotime, this interpretation is more likely. This implies that the distribution of Y, Th, and U in leucogranite is primarily controlled by the crystallization of accessory minerals such as zircon, monazite, and xenotime (e.g., Suzuki et al. 1992; Bea, 1996).

An alternative interpretation is that the CHIME ages of the two contrasting monazite types are indistinguishable due to a very rapid cooling rate of the leucogranite. The scenario assumes that the contrasting monazite grains grew at different temperatures,

and the huttonite-rich monazite grains were recrystallized during post-magmatic fluid alteration processes. Fluid-induced monazite alteration can occur at temperatures as low as 400-500°C (Williams et al. 2011). In contrast, melt crystallization occurred at 650-750°C (Imayama et al. 2012), and thus the crystallization of cheralite-rich monazite could have occurred at c. 650-750°C. Although the cooling rate of leucogranites in the Himalaya is still controversial, multi-system thermochronology (U–Pb monazite, K–Ar muscovite dating, and fission track zircon) revealed very rapid cooling rates of ~200-350°C/Ma after emplacement (Searle et al. 1999). If these cooling rates are correct, the age difference between two-type monazite grains formed at the temperature interval of 400-750°C is as small as *c.* 1 to 2 Ma, which is within the error of the CHIME dating.

Magmatic and tectonic implications for Cenozoic Himalayan Orogeny

Based on P-T pseudosection and petrography the migmatites in far-eastern Nepal the leucogranites were produced by fluid-absent muscovite dehydration reaction of Ms + Pl + Qtz = Als + Kfs + melt (Imayama et al. 2012). The existence of garnet in leucogranite may indicate that the biotite dehydration reaction of Bt + Pl + Sil + Qtz = Grt + Kfs + melt also occurred to produce the Himalayan leucogranite at temperature above 800°C (cf. Le Breton and Thompson 1988). However, the absence of retrograde zoning such as Mn enrichment and Mg depletion in garnet rims in leucogranite L09 is in contrast to the significant retrogression of garnet porphyroblasts in the surrounding migmatites (e.g., Imayama et al. 2010). The absence of Y zoning in garnet in leucogranite L09 contrasts with the Y zoning observed in garnets in migmatites in the Himalaya (Kohn et al. 2005). These observations suggest that the unzoned garnet porphyroblasts in sample L09 crystallized directly from higher temperature melts, and

457 do not prograde metamorphic garnet derived from the metasediments.

458 Similar CHIME monazite ages of *c.* 18-16 Ma in three leucogranites supports the
459 idea of Imayama et al. (2012) of an Early Miocene period of intense magmatism and
460 intrusion of leucogranites into the sillimanite migmatite hosts at the higher structural
461 level of the HHCS in far-eastern Nepal. 18-16 Ma leucogranites with andalusite (Visoná
462 et al. 2012) and cordierite (Streule et al. 2010) that were produced at lower pressures
463 suggest that the HHCS were hot even at shallow levels in the crust, accompanied by
464 channel flow (e.g., Beaumont et al. 2004; Godin et al. 2006). Based on the comparison
465 of the P-T conditions between channel flow model (Jamieson et al. 2004) and the field
466 observations, the observed field temperature gradient is much lower than those
467 predicted in channel flow models, and the discrepancy could be resolved by taking into
468 account heat advection upwards by melt (Imayama et al. 2010; Groppo et al. 2012;
469 Spencer et al. 2012; Wang et al. 2013). The intense magmatic intrusion of leucogranites
470 during 18-16 Ma could have transferred a large amount of heat towards the structurally
471 higher level of the HHCS, and played a role in producing low or nearly no field
472 temperature gradients in the exhumed crust (Imayama et al. 2010).
473

474 **ACKNOWLEDGMENTS**

475 We wish to thank T. Kato and T. Takeshita for useful discussion. We also wish to thank
476 T. Kajizuka for assisting us for analyses. We greatly thank C. J. Hetherington, J. Allaz,
477 M. Streule, and B. Budzyn for their critical reviews and assistance with English. This
478 study was supported in part by grants from Center for Chronological Research, Nagoya
479 University and the Sasakawa Scientific Research Grant from the Japan Science Society.
480

REFERENCES CITED

Beaumont, C., Jamieson, R.A., Nguyen, M.H., and Medvedev, S. (2004) Crustal channel flows: 1. Numerical models with applications to the tectonics of the Himalayan-Tibetan orogen. Journal of Geophysical Research, 109, B06406, doi:10.1029/2003JB002809.

Bea, F. (1996) Residence of REE, Y, Th and U in granites and crustal protoliths; Implications for the chemistry of crustal melts. Journal of Petrology, 37, 521-552.

Bollinger, L., Henry, P., and Avouac, J. P. (2006) Mountain building in the Nepal Himalaya: thermal and kinematic model. Earth and Planetary Science Letters, 244, 58-71.

Brookfield, M.E. (1993) The Himalayan passive margin from Precambrian to Cretaceous. Sedimentary Geology, 84, 1–35.

Budzyń, B., Hetherington, C.J., Williams, M.I., Jercinovic, M.J., and Michalik, M. (2010) Fluid-mineral interactions and constraints on monazite alteration during metamorphism. Mineralogical Magazine, 74, 659-681.

Burchfiel, B.C., Chen, Z., Hodges, K.V., Liu, Y., Royden, L.H., Deng, C., and Xu, J. (1992) The south Tibetan detachment system, Himalayan orogen: extension contemporaneous with and parallel to shortening in a collisional mountain belt. Geological Society of American Special Paper, 269, 1–41.

Catlos, E.J., Harrison, T.M., Manning, C.E., Grove, M., Rai, S.M., Hubbard, M.S., and Upreti, B.N. (2002) Records of the evolution of the Himalayan orogen from *in situ* Th-Pb ion microprobe dating of monazite: Eastern Nepal and western Garhwal. Journal of Asian Earth Science, 20, 459-479.

Cawood, P.A., Johnson, M.R.W., and Nemchin, A.A. (2007) Early Paleozoic orogenesis

along the Indian margin of Gondwana: Tectonic response to Gondwana assembly. Earth and Planetary Science Letter, 255, 70–84.

Corfu, F., Hanchar, J.M., and Hoskin, P.W.O. (2003) Atlas of Zircon Textures. In: J.M. Hanchar, and P.W.O. Hoskin, Eds., Zircon, 53, p. 469–500. Reviews in Mineralogy and Geochemistry, Mineralogical Society of America, Chantilly, Virginia.

Copeland, P., Parrish, R.R., and Harrison, T.M. (1988) Identification of inherited radiogenic Pb in monazite and its implications for U-Pb systematic. Nature, 333, 760-763.

DeCelles, P.G., Gehrels, G.E., Quade, J., LeReau, B., and Spurlin, M. (2000) Tectonic implications of U–Pb zircon ages of the Himalayan orogenic belt in Nepal. Science, 288, 497-499.

France-Lanord, C. and Le Fort, P. (1988) Crustal melting and granite genesis during the Himalayan collision orogenesis. Royal Society of Edinburgh Transactions. Earth Sciences, 79, 183-195.

Gehrels, G.E., DeCelles, P.G., Ojha, Y.P., and Upreti, B.N. (2006) Geologic and U‐Th‐Pb geochronologic evidence for early Paleozoic tectonism in the Kathmandu thrust sheet, central Nepal Himalaya. Geological Society American Bulletin, 118, 185–198.

Gehrels, G., Kapp, P., DeCelles, P., Pullen, A., Blakey, R., Weislogel, A., Ding, L., Guynn, J., Martin, A., McQuarrie, N., and Yin, A. (2011) Detrital zircon geochronology of pre-Tertiary strata in the Tibetan-Himalayan orogen. Tectonics, 30, doi:10.1029/2011TC002868.

Geisler, T., Schaltegger, U., and Tomaschek, F. (2007) Re-equilibration of zircon in aqueous fluids and melts. Elements, 3, 43-50.

529 Godin, L., Parrish, R.R., Brown, R.L., and Hodges, K.V. (2001) Crustal thickening
530 leading to exhumation of the Himalayan metamorphic core of central Nepal: insight
531 from U-Pb geochronology and $^{40}Ar/^{39}Ar$ thermochronology. Tectonics, 20, 729-747.
532 Godin, L., Grujic, D., Law, R.D., and Searle, M.P. (2006) Channel flow, ductile
533 extrusion and exhumation in continental collision zones: an introduction. In: R. D.
534 Law, M.P. Searle, and L., Godin, Eds., Channel Flow, Ductile Extrusion and
535 Exhumation in Continental Collision Zones, 268, p. 1–23, Special Publications,
536 Geological Society of London, London.
537 Goscombe, B., Gray, D. and Hand, M. (2006) Crustal architecture of the Himalayan
538 metamorphic front in eastern Nepal. Gondwana Research, 10, 232-255.
539 Groppo, C., Rubatto, D., Rolfo, F., and Lombardo, B. (2010) Early Oligocene partial
540 melting in the Main Central Thrust Zone (Arun valley, eastern Nepal Himalaya).
541 Lithos, 118, 287–301.
542 Groppo, C., Rolfo, F., and Indares, A. (2012) Partial melting in the Higher Himalayan
543 Crystallines of eastern Nepal: the effect of decompression and implications for the
544 'channel flow' model. Journal of Petrology, 0, 1-32.
545 Harris, N. and Massey, J. (1994) Decompression and anatexis of Himalayan metapelites.
546 Tectonics, 13, 1537-1546.
547 Harrison, T.M., McKeegan, K.D., and LeFort, P. (1995) Detection of inherited monazite
548 in the Manaslu leucogranite by $^{208}Pb/^{232}Th$ ion microprobe dating: Crystallization
549 age and tectonic implications. Earth and Planetary Science Letters, 133, 271-282.
550 Harrison, T.M., Grove, M., McKeegan, K.D., Coath, C.D., Lovera, O.M., and Le Fort, P.
551 (1999) Origin and episodic emplacement of the Manaslu intrusive complex, central
552 Himalaya. Journal of Petrology, 40, 3-19.

553 Harrison, T.M., Catlos, E.J., and Montel, J.M. (2002) U-Th-Pb dating of phosphate
554 minerals. In M.J. Kohn, J. Rakovan, and J.M. Hughes, Eds., Phosphates:
555 Geochemical, Geobiological, and Materials Importance, 48, p. 523–558. Reviews in
556 Mineralogy and Geochemistry, Mineralogical Society of America, Chantilly,
557 Virginia.
558 Hetherington, C.J., Jercinovic, M.J., Williams, M.L., and Mahan, K. (2008)
559 Understanding geologic processes with xenotime: Composition, chronology, and a
560 protocol for electron probe microanalysis. Chemical Geology, 254, 133-147.
561 Hodges, K., Bowring S., Davidek, K., Hawkins, D., and Krol, M. (1998) Evidence for
562 rapid displacement on Himalayan normal faults and the importance of tectonic
563 denudation in the evolution of mountain ranges. Geology, 26, 483-486.
564 Hodges, K.V. (2000) Overview: Tectonics of the Himalaya and southern Tibet from two
565 perspectives. Geological Society of American Bulletin, 112, 324-350.
566 Inger, S. and Harris, N. (1993) Geochemical constraints on leucogranite magmatism in
567 the Langtang Valley, Nepal Himalaya. Journal of Petrology, 3, 345-368.
568 Imayama, T., Takeshita, T., and Arita, K. (2010) Metamorphic P–T profile and P–T path
569 discontinuity across the far-eastern Nepal Himalaya: investigation of channel flow
570 models. Journal of Metamorphic Geology, 28, 527–549.
571 Imayama, T., Takeshita, T., Yi, K., Cho, D.-L., Lee, Y., Kitajima, K., Yagi, K., Tsutsumi,
572 Y., Kayama, M., Nishido, H., Okumura, T., Itaya, T., and Sano, Y. (2012) Two-stage
573 partial melting and contrasting cooling rates within the Higher Himalayan
574 Crystalline Sequences in the far-eastern Nepal Himalaya. Lithos, 134-135, 1-22.
575 Jamieson, R.A., Beaumont, C., Medvedev, S., and Nguyen, M.H. (2004) Crustal
576 channel flows: 2. Numerical models with implications for metamorphism in the

Himalayan–Tibetan orogen. Journal of Geophysical Research, 109, B06407, doi:10.1029/2003JB002811.

Jercinovic, M.J. and Williams, M.L. (2005) Analytical perils (and progress) in electron microprobe trace analysis applied to geochronology: Background acquisition, interferences, and beam irradiation effects. American Mineralogists, 90, 526-546.

Kretz, R. (1983) Symbols for rock-forming minerals. American Mineralogist, 68, 277–279.

Kohn, M.J., Wieland, M.S., Parkinson, C.D., and Upreti, B.N. (2004) Miocene faulting at plate tectonic velocity in the Himalaya of central Nepal: Earth and Planetary Science Letters, 228, 299-310.

Kohn, M.J., Wieland, M.S., Parkinson, C.D., and Upreti, N. (2005) Five generations of monazite in Langtang genisses: implications for chronology of the Himalayan metamorphic core. Journal of Metamorphic Geology, 23, 399-406.

Kohn, M. J. (2008) P-T-t data from central Nepal support critical taper and repudiate large-scale channel flow of the Greater Himalayan Sequence. Geological Society of America Bulletin, 120, 259-273.

Le Breton, N. and Thompson, A.B. (1988) Fluid-absent (dehydration) melting of biotite in metapelites in early stages of crustal anatexis. Contributions to Mineral and Petrology, 99, 226-237.

Le Fort, P., Debon, F., Pêcher, A., Sonet, J., and Vidal, P. (1986) The 500 Ma magmatic event in Alpine southern Asia, a thermal episode at Gondwana scale. Sciences de la Terre. Mémoires 47, 191–209.

Martin, A.J., DeCelles, P.G., Gehrels, G.E., Patchett, P.J., and Isachsen, C. (2005) Isotopic and structural constraints on the location of the Main Central thrust in the

Annapurna Range, central Nepal Himalaya. Geological Society of America Bulletin, 117, 926–944.

Murphy, M.A. and Harrison, T.M. (1999) Relationship between leucogranites and the Qomolangma detachment in the Rongbuk Valley, south Tibet. Geology, 27, 831-834.

Myrow, P.M., Hughes, N.C., Paulsen, T.S., Williams, I.S., Thomson, K.R., Bowring, S.A., Peng, S.C., Ahluwalia, A.D. (2003) Integrated tectonostratigraphic reconstruction of the Himalaya and implications for its tectonic reconstruction. Earth Planetary Science Letters, 212, 433–441.

Noble, S.R., Searle, M.P., and Walker, C.B. (2001) Age and tectonic significance of Permian granites in western Zansker, High Himalaya. Journal of Geology, 109, 127-135.

Parrish, R.R. and Hodges, K.V. (1996) Isotopic constrains on the age and provenance of the Lesser and Greater Himalayan sequences, Nepalese Himalaya. Geological Society of America Bulletin, 108, 904-911.

Pichavant, M., Costa, F., Burgisser, A., Scaillet, B., Martel, C., and Poussineau, S. (2007) Equilibration Scales in Silicic to Intermediate Magmas—Implications for Experimental Studies. Journal of Petrology, 48, 1955-1972.

Pyle, J.M., Spear, F.S., Rudnick, R.L., and McDonough, W.F. (2001) Monazite-xenotime-garnet equilibrium in metapelites and a new monazite-garnet thermometer. Journal of Petrology, 42, 2083–2107.

Pyle, J.M. and Spear, F.S. (2003) Four generations of accessoryphase growth in low-pressure migmatites from SW New Hampshire. American Mineralogist, 88, 338–351.

Sakai, H. (1991) The Gonwanas in the Nepal Himalaya. In: S.K. Tandon, C.C. Pant, and

S.M. Casshyap, Eds, Sedimentary Basins of India: Tectonic Context. pp. 202–217, Gyanodaya Prakashan, Nainital, India.

Schärer, U. (1984) The effect of initial ^{230}Th disequilibrium on young U-Pb ages: the Makalu case, Himalaya. Earth and Planetary Science Letter, 67, 191-204.

Schelling, D. (1992) The tectonostratigraphy and structure of the eastern Nepal Himalaya. Tectonics, 11, 925-943.

Searle, M.P., Noble, S.R., Hurford, A.J., and Rex, D.C. (1999) Age of crustal melting, emplacement and exhumation history of the Shivling leucogranite, Garhwal Himalaya. Geological Magazine, 136, 513-525.

Searle, M.P., Simpson, R.L., Law, R.D., Parrish, R.R., and Waters, D.J. (2003) The structural geometry, metamorphic and magmatic evolution of the Everest massif, High Himalaya of Nepal–South Tibet. Journal of the Geological Society of London, 160, 345–366.

Simpson, R.L., Parrish, R.R., Searle, M.P., and Waters, D.J. (2000) Two episodes of monazite crystallization during metamorphism and crustal melting in the Everest region of the Nepalese Himalaya. Geology, 28, 403-406.

Spear, F.S. and Pyle, J.M. (2010) Theoretical modeling of monazite growth in a low-Ca metapelites. Chemical Geology, 273, 111-119.

Spencer, C.J., Harris, R.A., and Dorais, M. J., 2012. The metamorphism and exhumation of the Himalayan metamorphic core, eastern Garhwal region, India. Tectonics, 31, doi:10.1029/2010TC002853.

Spring, L., Bussy, F., Vannay, J.-C., Huon, S., and Cosca, M.A. (1993) Early Permian granitic dykes of alkaline affinity in the Indian High Himalaya of Upper Lahul and SE Zanskar: geochemical characterization and geotectonic implications. In Treloar,

649 P. J., and Searle, M. P., Eds. Himalayan tectonics. Geological Society London
650 Special Issue, 74, 251–264.
651 Streule, M.J., Searle, M.P., Waters, D.J., Matthew, S.A., and Horstwood, M.S.A. (2010)
652 Metamorphism, melting and channel flow in the Greater Himalaya Sequence and
653 Makalu leucogranite: constraints from thermobarometry, metamorphic modelling
654 and U–Pb geochronology. Tectonics, 29, TC5011,
655 http://dx.doi.org/10.1029/2009TC002533.
656 Suzuki K. and Adachi M. (1991) Precambrian provenance and Silurian metamorphism
657 of the Tsubonasawa paragneiss in the South Kitakami terrane, Northwest Japan,
658 revealed by the chemical Th-U-total Pb isochron ages of monazite, zircon and
659 xenotime. Geochemical Journal, 25, 357–76.
660 Suzuki, K., Adachi, M., Yamamoto, K., and Nakai, Y. (1992) Intra-grain distribution of
661 REE and crystallization sequence of accessory minerals in the Creraceous Busetsu
662 Granite at Okazaki, central Japan. Geochemical Journal, 26, 383-394.
663 Suzuki, K. and Kato, T. (2008) CHIME dating of monazite, xenotime, zircon and
664 polycrase: Protocol, pitfalls and chemical criterion of possibly discordant age data.
665 Gondwana Research, 14, 569-586.
666 Townsend, K.J., Miller, C.F., D'Andrea, J.L., Ayers, J.C., Harrison, T.M., and Coath,
667 C.D. (2000) Low temperature replacement of monazite in the Ireteba granite,
668 Southern Nevada: Geochronological implications. Chemical Geology, 172, 95-112.
669 Upreti, B.N. (1999) An overview of the stratigraphy and tectonics of the Nepal
670 Himalaya. Journal of Asian Earth Science, 17, 577-606.
671 Viskupic, K. and Hodges, K.V. (2001) Monazite-xenotime thermochronometry:
672 methodology and an example from the Nepalese Himalaya. Contributions to

673 Mineral and Petrology, 141, 233-247.
674 Viskupic, K., Hodges, K.V., and Bowring, S.A. (2005) Timescales of melt generation
675 and the thermal evolution of the Himalayan metamorphic core, Everest region,
676 eastern Nepal. Contributions to Mineral and Petrology, 149, 1-21.
677 Visonà, D., Carosi, R., Montomoli, C., Tiepolo, M., and Peruzzo, L. (2012) Miocene
678 andalusite leucogranites in central-east Himalaya (Everest-Masang Kang area):
679 Low-pressure melting during heating. Lithos, 144-145, 194-208.
680 Wang, J.M., Zhang, J.J., and Wang, X.X., 2013. Structural kinematics, metamorphic P-T
681 profiles and zircon geochronology across the Greater Himalayan Crystalline
682 Complex in south-central Tibet: implication for a revised channel flow. Journal of
683 Metamorphic Geology, doi: 10.1111/jmg.12036.
684 Williams, M.L., Jercinovic, M.J., and Hetherington, C.J. (2007) Microprobe monazite
685 geochronology: Understanding geologic processes by integrating composition and
686 chronology. Annual Review of Earth and Planetary Science, 35, 137-175.
687 Williams, M.L., Jercinovic, M.J., Harlov, D.E., Budzyń, B., Hetherington, C.J. (2011)
688 Resetting monazite ages during fluid-related alteration. Chemical Geology, 283,
689 218-225.
690

691 **Figure captions**

692

693 **FIGURE 1.** Geological map along the Tamor-Ghunsa transect of far-eastern Nepal,
694 showing location of samples used for CHIME age analyses. Modified after Goscombe
695 et al. (2006) and Imayama et al. (2010). Mineral abbreviations after Kretz (1983). Se:

696 sericite; Bg: bearing.

697

698 **FIGURE 2.** Photomicrographs of leucogranites and outcrop photograph from the
699 Tamor-Ghunsa section, far-eastern Nepal Himalaya. (a) Outcrop photograph of
700 garnet-bearing sillimanite-muscovite-biotite leucogranite (L09) intruded into
701 sillimanite-garnet-biotite migmatite. Note that the leucogranite cuts the foliation in the
702 migmatite. (b) Prismatic sillimanite and euhedral garnet porphyroblast in garnet-bearing
703 sillimanite-muscovite-biotite leucogranite (L09). (c) Outcrop photograph showing
704 massive and intercalated exposures of muscovite-biotite leucogranite L02 (d) Alteration
705 to chlorite of biotite flakes in muscovite-biotite leucogranite L02.

706

707 **FIGURE 3.** Photomicrograph, BSE image, and X-ray compositional maps of garnet
708 porphyroblast in garnet-bearing biotite-muscovite leucogranite L09.

709

710 **FIGURE 4.** (a) Co-existing monazite and euhedral zircon grains in garnet-bearing
711 biotite-muscovite leucogranite L09. (b) Photomicrograph of monazite grains clustered
712 with xenotime, (c) backscattered electron (BSE) image of monazite partly altered or
713 dissolved, and (d) BSE image of xenotime with oscillatory zoning in muscovite-biotite

714 leucogranite L02. Xtm: xenotime.

715

716 **FIGURE 5.** Zoning patterns revealed by BSE image and X-ray compositional maps of
717 monazite grains in garnet-bearing biotite-muscovite leucogranite L09 in far-eastern
718 Nepal. (a) Monazite grain 2, which display concentric zoning. (b) Monazite grain 15,
719 showing prominent compositional zoning with Y-rich core, (c) Monazite grain 11,
720 showing prominent compositional zoning in Y content. (d) Monazite grain 18, which
721 display patchy zoning in Y content. Solid circles indicate the locations of spot analyses.
722 Numerals show apparent chemical age for a single spot. C: core, M: mantle, R: rim.

723

724 **FIGURE 6.** Diagrams of (a) CaO content plotted against (ThO_2 + UO_2) content, (b)
725 SiO_2 content plotted against (ThO_2 + UO_2) content, (c) Y_2O_3 vs. PbO, and (d) Y_2O_3 vs.
726 UO_2 in monazite grains from garnet-bearing sillimanite-muscovite-biotite leucogranite
727 L09 in far-eastern Nepal. Data of different monazite domains are plotted as shown in
728 legends.

729

730 **FIGURE 7.** PbO (wt. %) vs. ThO_2* (wt. %) plots of (a) core and (b) mantle, rim, and
731 patchy-zoned domains in monazite in garnet-bearing sillimanite-biotite-muscovite

leucogranite L09. Dashed lines represent the reference isochrones of 450 Ma, 325 Ma, and 285 Ma. Solid line shows an isochron of overgrown rim in monazites and patchy-zoned grains with the age (± 2 σ errors). Bar is analytical uncertainty (2σ) for spot analyses of PbO content. Data of different monazite domains are plotted as shown in legends.

FIGURE 8. (a) Zoning patterns revealed by BSE image and X-ray compositional maps of monazite grain 2 in muscovite-biotite leucogranite L02. BSE images and X-ray compositional maps of (b) monazite grain 7 and xenotime grain 1and (c) monazite grain 8 in sample L02. In BSE image, monazite grains are brighter than xenotime. For locations of Fig. 8a and b, see Fig. 3c. Solid circles indicate the locations of spot analyses. Numerals show apparent chemical age for a single spot.

FIGURE 9. Diagrams of (a) CaO content plotted against (ThO_2 + UO_2) content, (b) Y_2O_3 vs. UO_2, and (c) SiO_2 content plotted against (ThO_2 + UO_2) content in monazite grains from muscovite-biotite leucogranite L02 in far-eastern Nepal.

FIGURE 10. PbO (wt. %) vs. ThO_2* (wt. %) plots of (a) monazite and (b) xenotime

750 grains in biotite-muscovite leucogranite L02. Each line in figures shows the isochron of
751 eight monazite grains and four xenotime grains with age (± 2 σ errors) respectively. Bar
752 is analytical uncertainty (2σ) for spot analyses of PbO content.

753

754 **FIGURE 11**. Zoning patterns revealed by BSE image and X-ray compositional maps of
755 monazite grain 2 in aplitic leucogranite L05. Solid circles indicate the locations of spot
756 analyses. Numerals show apparent chemical age for a single spot.

757

758 **FIGURE 12.** Diagrams of (a) CaO content plotted against (ThO_2 + UO_2) content and
759 (b) SiO_2 content plotted against (ThO_2 + UO_2) content in analyzed monazite from
760 sample L05. Data of different monazite grains are plotted as shown in legends.

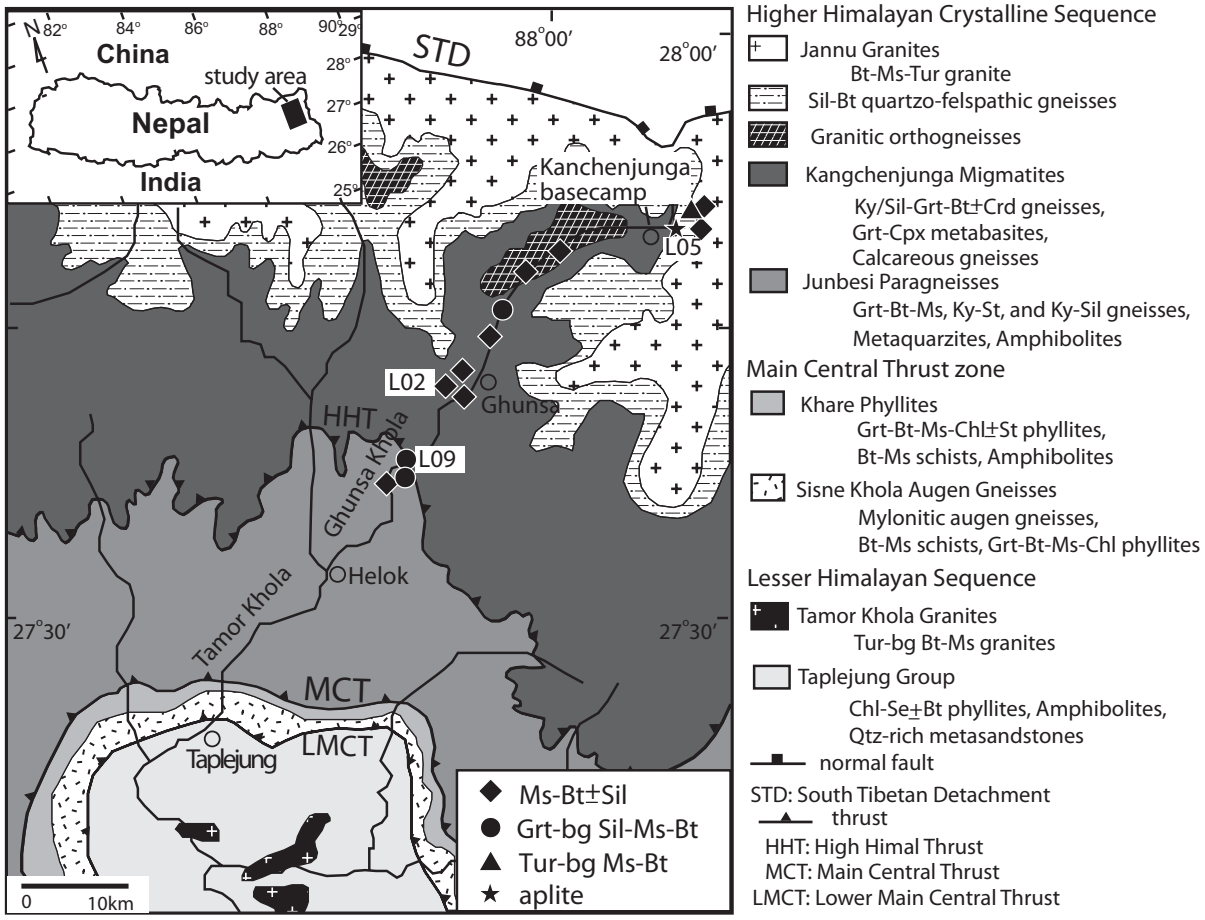
82°
84°
86°
88°
90°
29°
28°
27°
26°
25°
China
study area
Nepal
India
STD
88°00′
28°00′
Kanchenjunga
basecamp
L05
L02
Ghunsa
HHT
Ghunsa Khola
L09
Helok
Tamor Khola
27°30′
27°30′
MCT
LMCT
Taplejung
0
10km
Ms-Bt±Sil
Grt-bg Sil-Ms-Bt
Tur-bg Ms-Bt
aplite
Higher Himalayan Crystalline Sequence
Jannu Granites
Bt-Ms-Tur granite
Sil-Bt quartzo-felspathic gneisses
Granitic orthogneisses
Kangchenjunga Migmatites
Ky/Sil-Grt-Bt±Crd gneisses,
Grt-Cpx metabasites,
Calcareous gneisses
Junbesi Paragneisses
Grt-Bt-Ms, Ky-St, and Ky-Sil gneisses,
Metaquarzites, Amphibolites
Main Central Thrust zone
Khare Phyllites
Grt-Bt-Ms-Chl±St phyllites,
Bt-Ms schists, Amphibolites
Sisne Khola Augen Gneisses
Mylonitic augen gneisses,
Bt-Ms schists, Grt-Bt-Ms-Chl phyllites
Lesser Himalayan Sequence
Tamor Khola Granites
Tur-bg Bt-Ms granites
Taplejung Group
Chl-Se±Bt phyllites, Amphibolites,
Qtz-rich metasandstones
normal fault
STD: South Tibetan Detachment
thrust
HHT: High Himal Thrust
MCT: Main Central Thrust
LMCT: Lower Main Central Thrust

Fig. 1

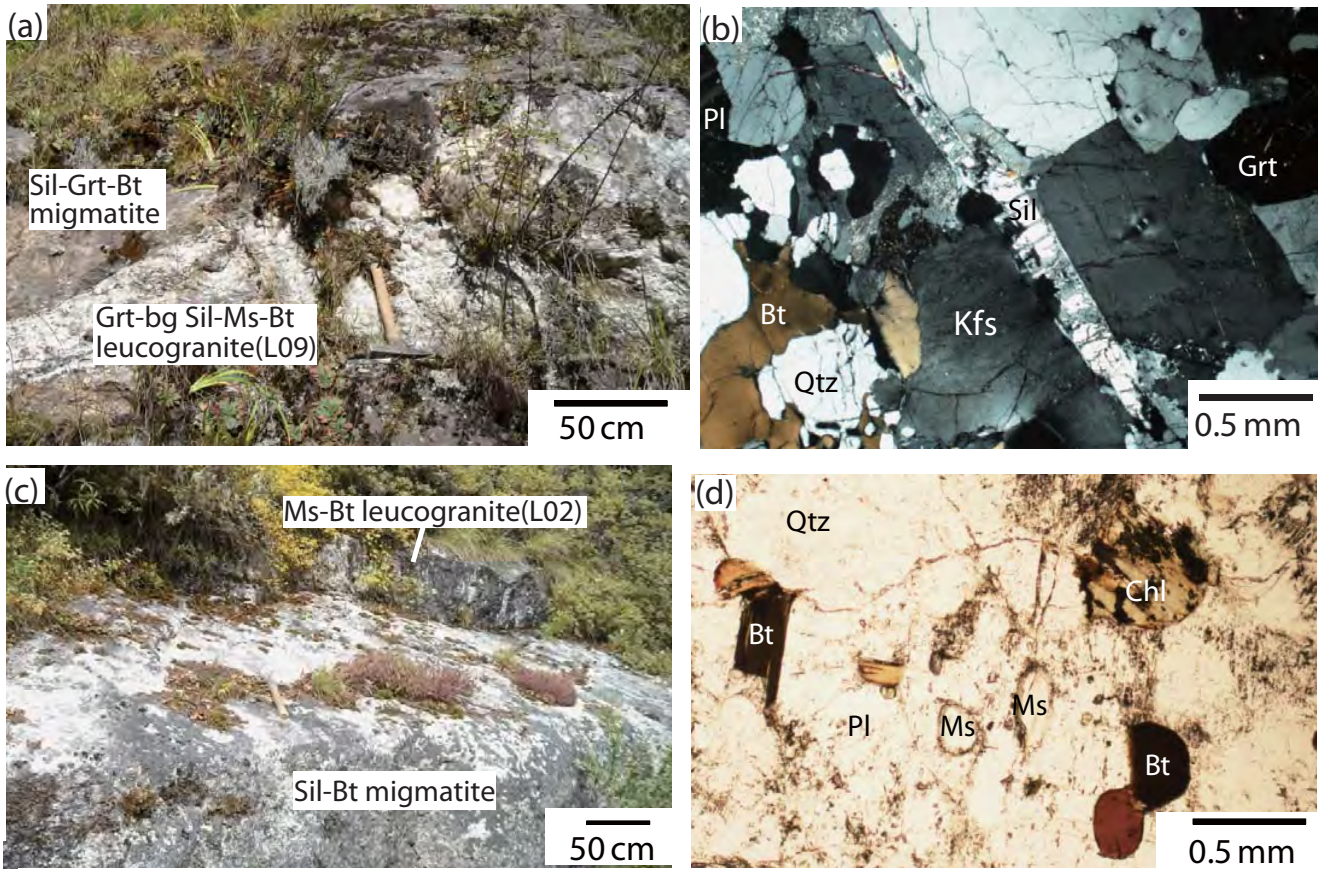
(a)
Sil-Grt-Bt migmatite
Grt-bg Sil-Ms-Bt leucogranite(L09)
50 cm
(b)
Pl
Grt
Sil
Bt
Kfs
Qtz
0.5 mm
(c)
Ms-Bt leucogranite(L02)
Sil-Bt migmatite
50 cm
(d)
Qtz
Chl
Bt
Pl
Ms
Ms
Bt
0.5 mm

Fig. 2

This is a preprint, the final version is subject to change, of the American Mineralogist (MSA)
Cite as Authors (Year) Title. American Mineralogist, in press.
(DOI will not work until issue is live.) DOI: http://dx.doi.org/10.2138/am.2014.4267

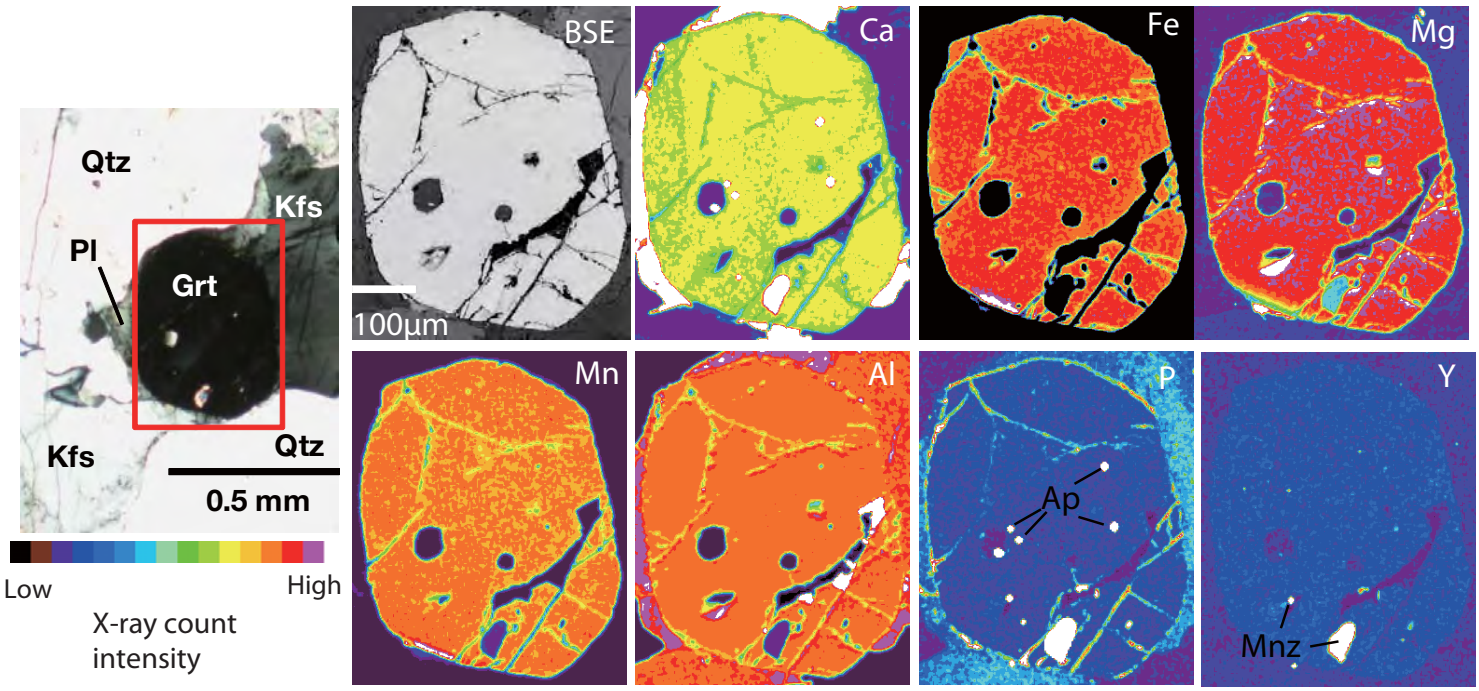

Fig. 3

This is a preprint, the final version is subject to change, of the American Mineralogist (MSA)
Cite as Authors (Year) Title. American Mineralogist, in press.
(DOI will not work until issue is live.) DOI: http://dx.doi.org/10.2138/am.2014.4267

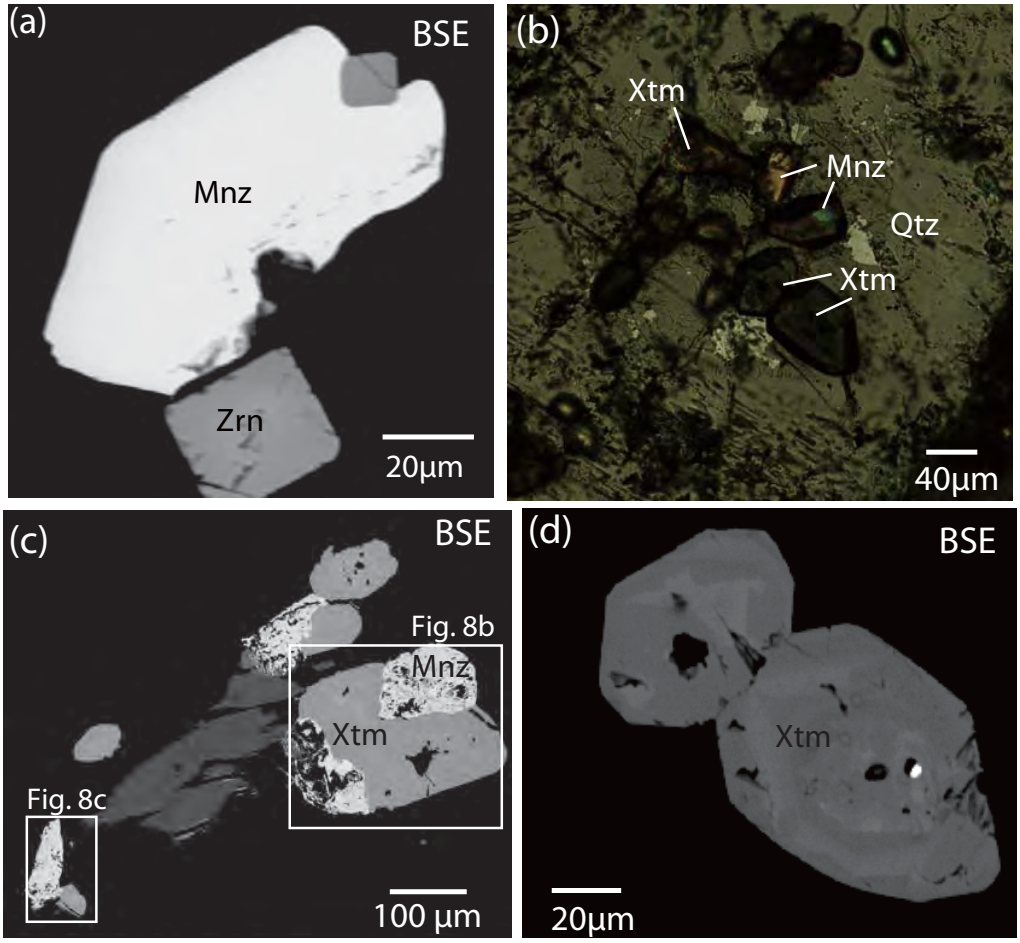

Fig. 4

This is a preprint, the final version is subject to change, of the American Mineralogist (MSA)
Cite as Authors (Year) Title. American Mineralogist, in press.
(DOI will not work until issue is live.) DOI: http://dx.doi.org/10.2138/am.2014.4267

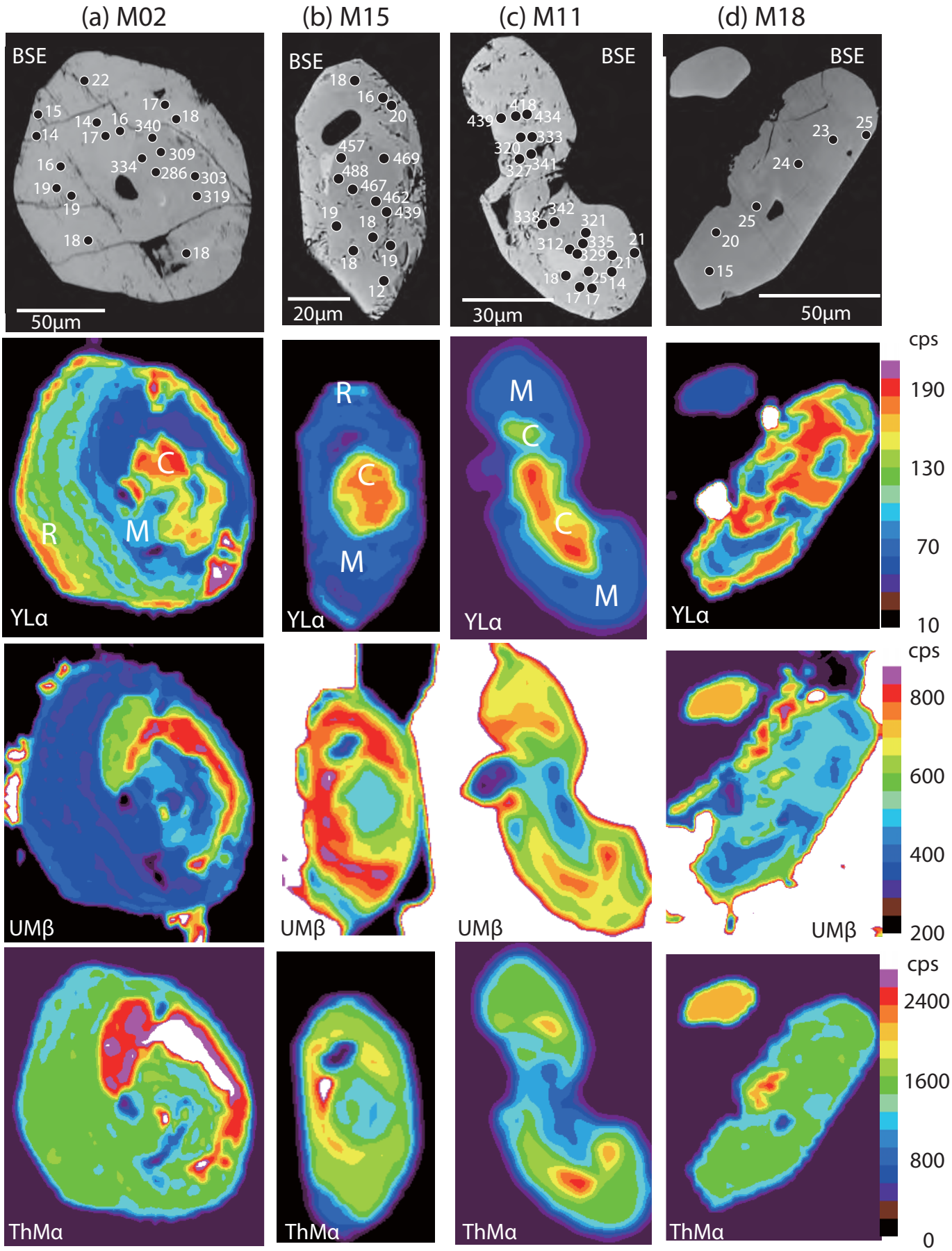

Fig. 5

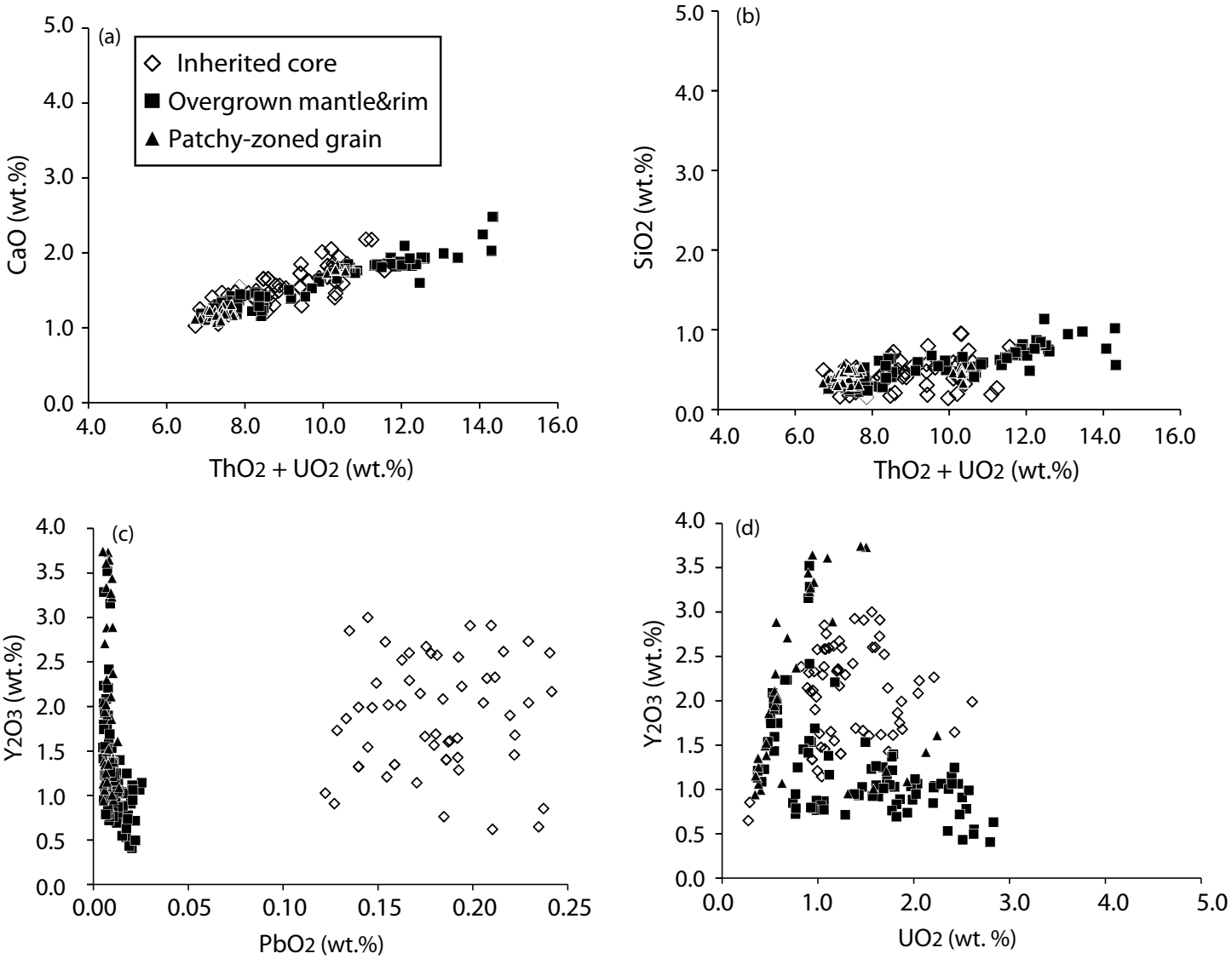
(a)
Inherited core
Overgrown mantle&rim
Patchy-zoned grain
CaO (wt.%)
ThO2 + UO2 (wt.%)
(b)
SiO2 (wt.%)
ThO2 + UO2 (wt.%)
(c)
Y2O3 (wt.%)
PbO2 (wt.%)
(d)
Y2O3 (wt.%)
UO2 (wt. %)

Fig. 6

This is a preprint, the final version is subject to change, of the American Mineralogist (MSA)
Cite as Authors (Year) Title. American Mineralogist, in press.
(DOI will not work until issue is live.) DOI: http://dx.doi.org/10.2138/am.2014.4267

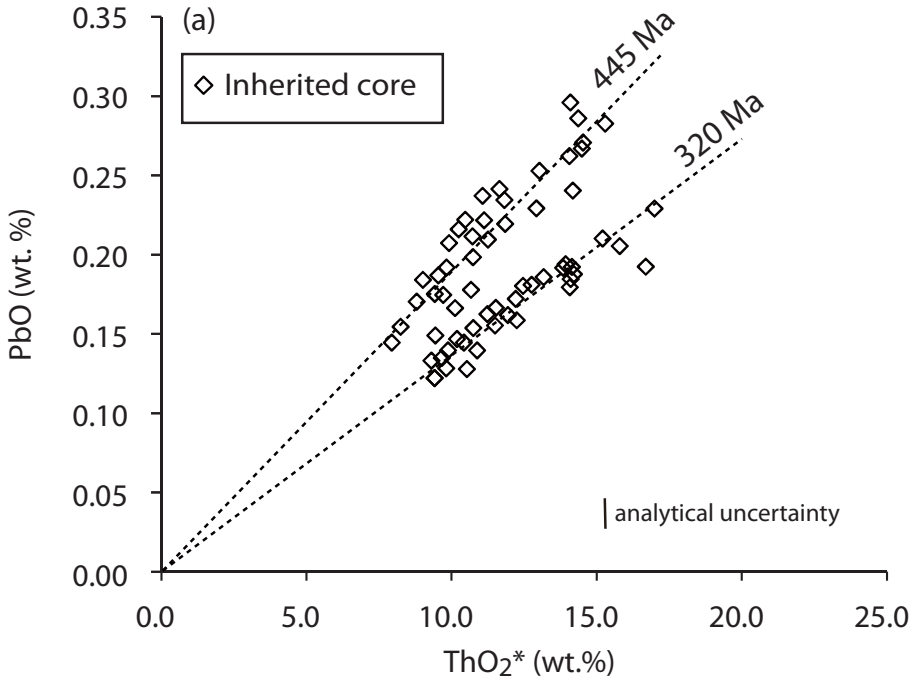

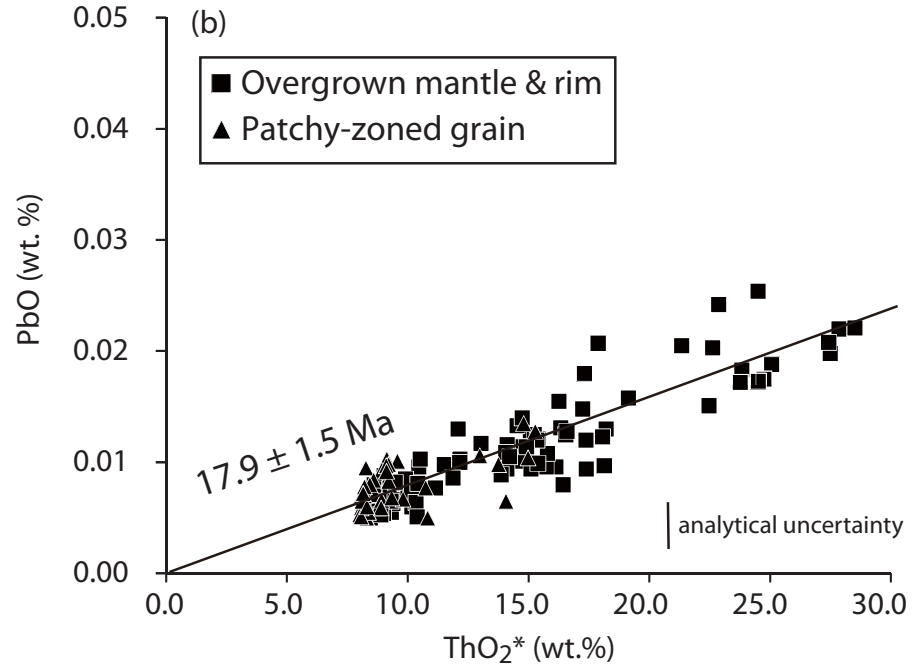

Fig. 7

This is a preprint, the final version is subject to change, of the American Mineralogist (MSA)
Cite as Authors (Year) Title. American Mineralogist, in press.
(DOI will not work until issue is live.) DOI: http://dx.doi.org/10.2138/am.2014.4267

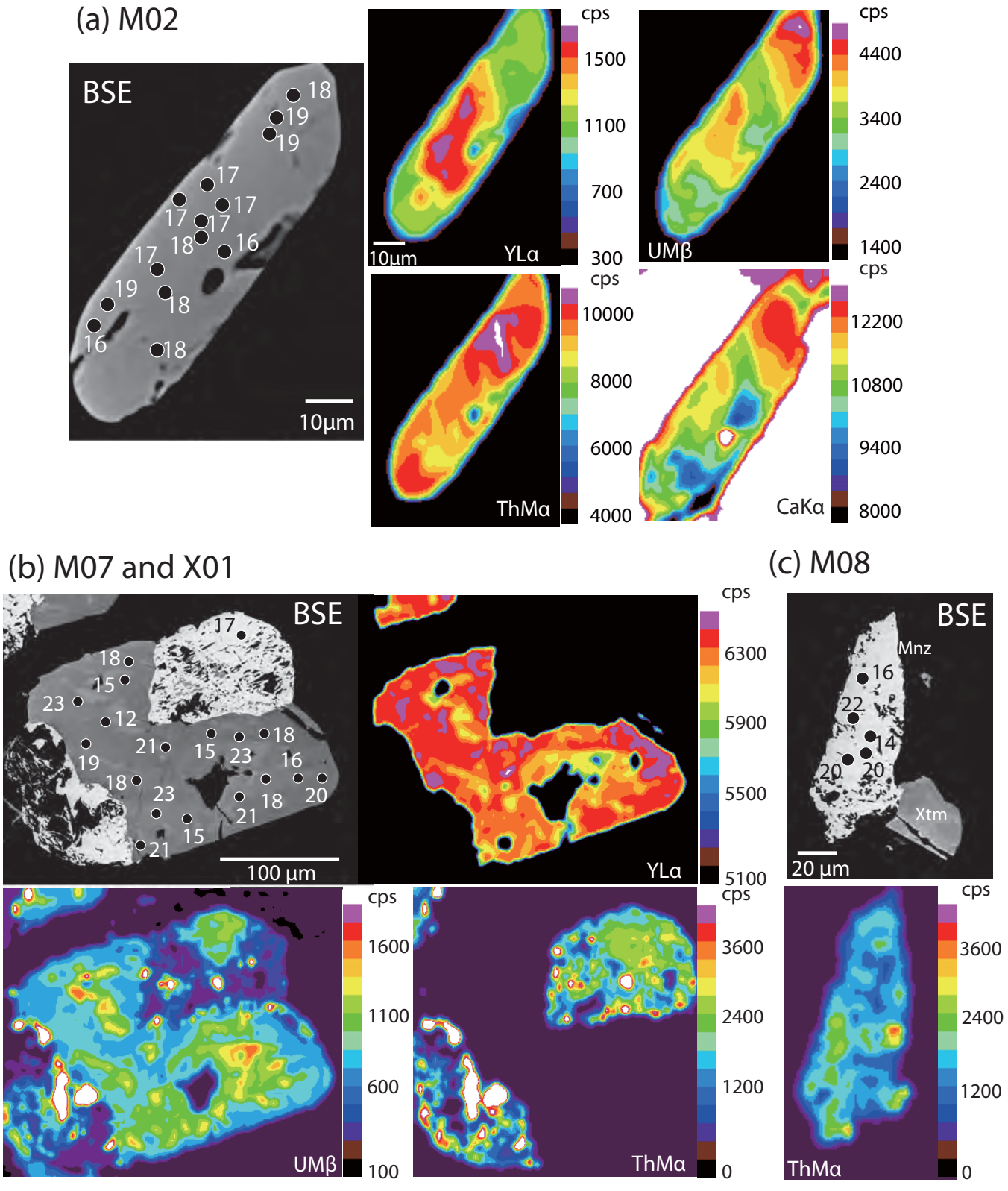

Fig. 8

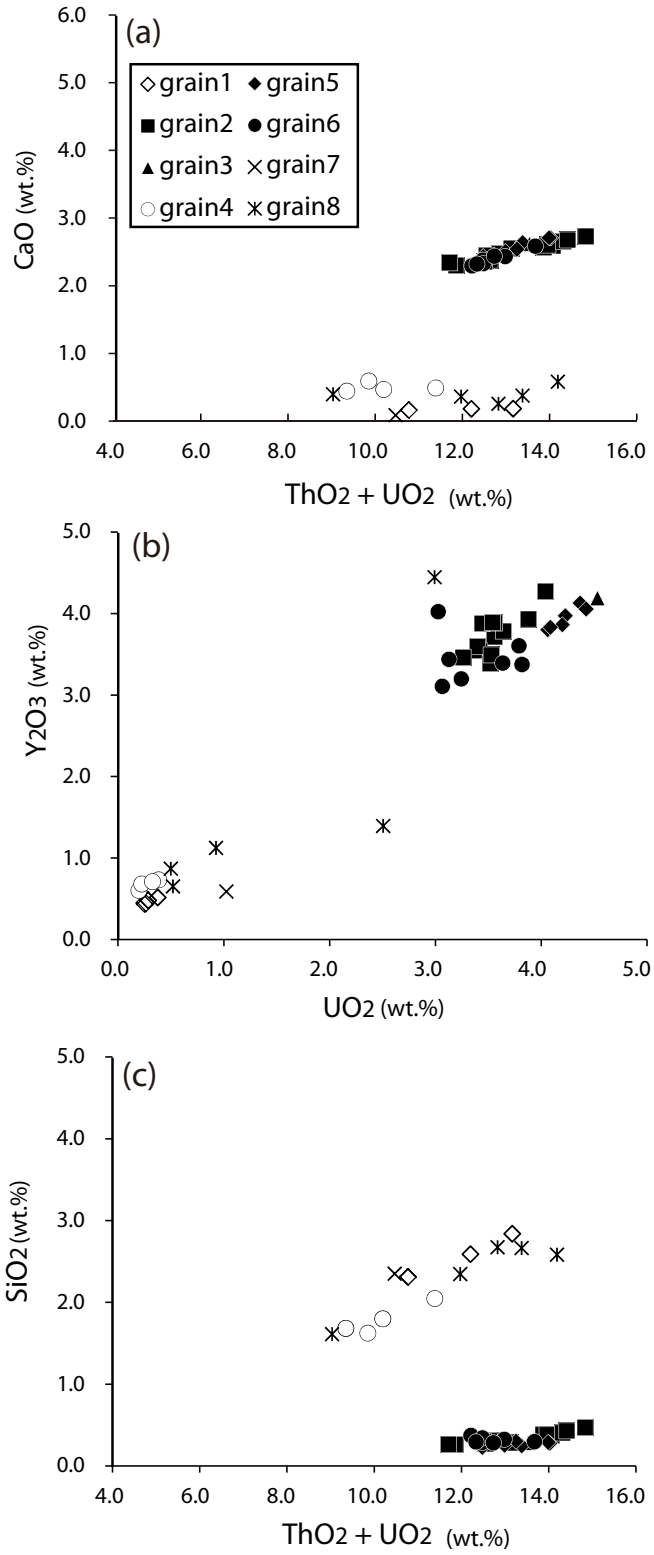
(a)
grain1
grain2
grain3
grain4
grain5
grain6
grain7
grain8
CaO (wt.%)
ThO2 + UO2 (wt.%)
(b)
Y2O3 (wt.%)
UO2 (wt.%)
(c)
SiO2 (wt.%)
ThO2 + UO2 (wt.%)

Fig. 9

This is a preprint, the final version is subject to change, of the American Mineralogist (MSA)
Cite as Authors (Year) Title. American Mineralogist, in press.
(DOI will not work until issue is live.) DOI: http://dx.doi.org/10.2138/am.2014.4267

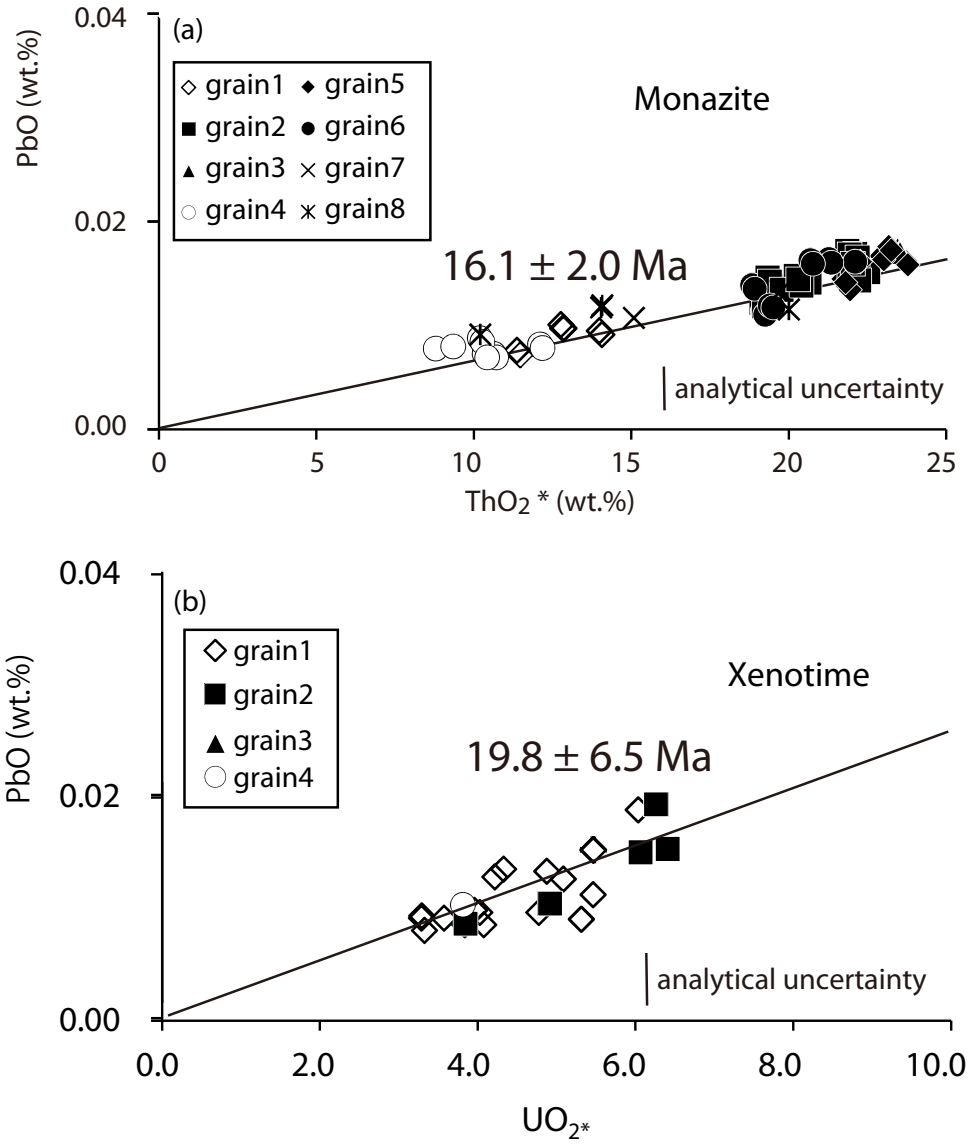

Fig. 10

This is a preprint, the final version is subject to change, of the American Mineralogist (MSA)
Cite as Authors (Year) Title. American Mineralogist, in press.
(DOI will not work until issue is live.) DOI: http://dx.doi.org/10.2138/am.2014.4267

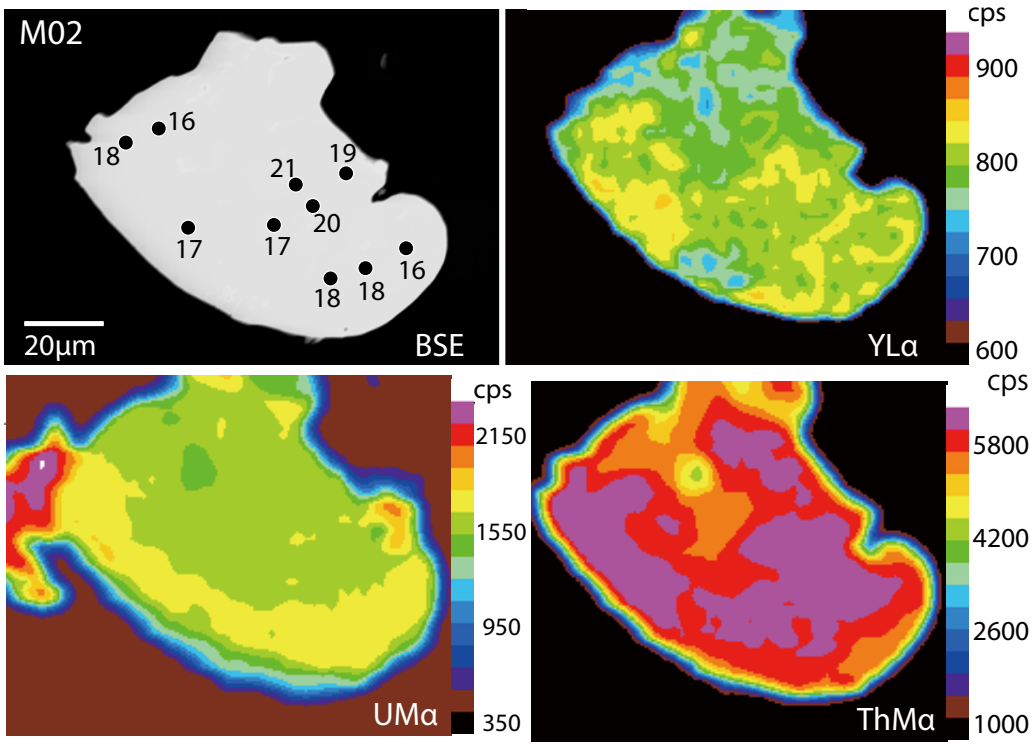

Fig. 11

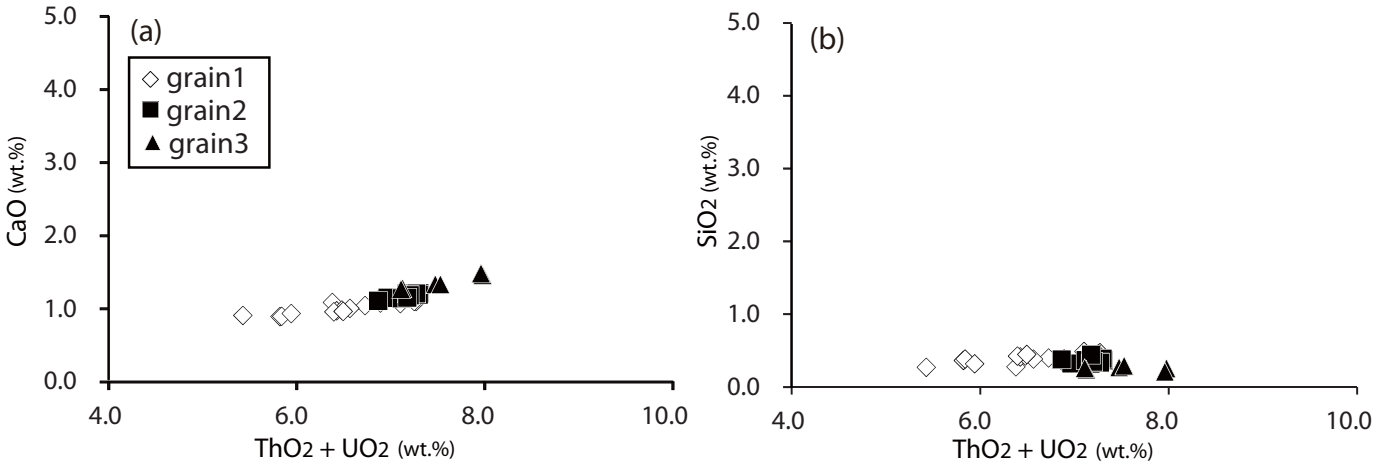
(a)
grain1
grain2
grain3
CaO (wt.%)
ThO2 + UO2 (wt.%)
5.0
4.0
3.0
2.0
1.0
0.0
4.0
6.0
8.0
10.0
(b)
SiO2 (wt.%)
ThO2 + UO2 (wt.%)

Fig. 12

TABLE 1. Representative electron microprobe analyses of ThO_2, UO_2, PbO, CaO, Y_2O_3, S, and SiO_2 (wt.%) of monazites in leucogranites, far-eastern Nepal

spots	ThO_2	UO_2	PbO_2	Age (Ma)	ThO_2*	CaO	Y_2O_3	S	SiO_2	(Ca+Si)/(Th+U+Pb+S)
Sample L09										
M02-04	11.347	1.117	0.0114	18	14.910	1.60	1.17	nd	1.13	1.00
M02-06	12.251	1.821	0.0123	16	18.056	2.25	0.69	0.002	0.77	0.99
M02-09	6.693	1.165	0.1271	286	10.481	1.55	1.55	nd	0.15	1.00
M02-10	7.404	1.066	0.1397	303	10.874	1.66	2.85	0.003	0.17	0.99
M02-21	12.554	1.771	0.0130	17	18.202	2.48	0.76	nd	0.56	0.99
M02-23	6.576	0.993	0.1284	309	9.809	1.44	2.58	0.003	0.22	1.00
M02-27	7.304	1.285	0.1554	319	11.491	1.65	2.29	nd	0.21	1.00
M02-30	6.187	1.223	0.1469	340	10.179	1.47	2.68	nd	0.18	1.02
M02-31	5.965	1.197	0.1397	334	9.870	1.41	2.33	nd	0.16	1.00
M05-03	9.719	1.776	0.0099	15	15.379	1.81	1.22	0.011	0.65	0.98
M05-04	7.379	1.114	0.2372	504	11.061	1.31	2.60	nd	0.67	1.04
M05-09	7.492	0.927	0.096	21	10.449	1.15	1.53	0.003	0.64	0.98
M05-11	6.729	1.063	0.2161	496	10.239	1.36	2.38	0.001	0.40	1.02
M05-12	6.453	0.983	0.1349	330	9.658	1.27	2.04	0.003	0.43	1.03
M05-18	9.028	1.789	0.0140	22	14.732	1.73	1.40	nd	0.57	0.99
M05-19	6.516	0.889	0.1222	306	9.411	1.23	2.15	0.006	0.37	0.98
M05-22	8.565	1.771	0.0105	17	14.212	1.69	1.37	0.004	0.52	0.99
M11-01	9.109	2.201	0.0096	14	16.125	1.84	0.85	nd	0.62	1.01
M11-02	16.246	2.355	0.0172	17	23.756	2.08	0.53	0.001	2.02	1.00
M11-03	17.048	2.511	0.0188	17	25.054	2.15	0.43	0.005	2.20	1.01
M11-05	8.928	1.285	0.0117	21	13.026	1.73	0.72	nd	0.48	1.01
M11-07	8.604	1.657	0.2623	439	14.052	1.86	1.62	0.001	0.42	1.00
M11-09	7.413	1.469	0.1722	333	12.206	1.57	1.67	nd	0.41	1.01
M11-10	8.620	1.783	0.2670	434	14.482	1.94	1.61	0.002	0.32	0.99
M11-11	7.880	1.533	0.2293	418	12.916	1.73	1.61	0.003	0.31	0.98
M11-12	7.393	1.394	0.1620	320	11.935	1.57	1.69	0.007	0.41	1.02
M11-13	5.597	1.134	0.1332	338	9.299	1.03	1.65	0.005	0.50	1.01
M11-14	13.693	2.798	0.0203	21	22.615	2.42	0.41	0.005	1.12	0.99
M11-15	8.070	1.562	0.1859	333	13.166	1.62	3.00	0.011	0.53	1.00
M11-16	15.008	2.462	0.0242	25	22.862	2.01	1.07	0.005	1.88	1.01
M11-17	15.696	2.549	0.0183	18	23.822	2.01	0.78	0.002	2.09	1.02
M11-18	7.929	1.478	0.1811	335	12.753	1.55	2.91	0.005	0.57	1.02
M11-19	8.857	1.643	0.1878	312	14.208	1.59	2.73	0.005	0.74	1.00
M11-20	7.085	1.645	0.1804	342	12.456	1.31	2.91	0.011	0.61	0.98
M11-21	7.004	1.383	0.1665	341	11.517	1.40	2.93	0.004	0.48	1.01
M11-22	8.626	1.692	0.1924	321	14.141	1.62	2.52	0.005	0.63	0.98
M11-23	8.720	1.596	0.1941	329	13.926	1.46	2.60	0.011	0.95	1.04
M11-24	8.724	1.569	0.1918	327	13.840	1.40	2.60	0.009	0.95	1.02
M11-26	6.354	1.246	0.1446	327	10.418	1.23	2.60	0.009	0.49	1.02
M15-01	10.296	1.971	0.0128	18	16.579	1.83	1.04	0.005	0.87	1.01
M15-05	8.359	1.049	0.2346	467	11.815	1.54	2.29	0.006	0.48	0.96
M15-07	10.296	1.718	0.0108	16	15.774	1.84	1.06	nd	0.68	0.97
M15-12	7.421	1.163	0.2096	439	11.247	1.45	2.62	0.003	0.44	0.99

M15-13	10.411	1.461	0.0123	19	15.068	1.82	1.03	0.005	0.76	1.00
M15-16	10.161	2.218	0.0148	20	17.234	1.85	1.04	0.005	0.84	1.00
M15-17	10.084	2.286	0.0120	16	17.373	1.85	1.07	0.005	0.84	1.00
M15-18	11.287	2.178	0.0551	71	18.257	1.95	1.33	0.004	0.87	0.96
M15-19	7.600	1.067	0.2218	469	11.116	1.42	2.59	0.005	0.50	0.99
M15-20	7.140	1.086	0.2116	464	10.717	1.41	2.76	nd	0.40	1.00
M15-21	10.027	1.427	0.0114	18	14.577	1.82	0.98	0.003	0.65	1.00
M15-22	9.848	2.364	0.0094	12	17.382	1.93	1.01	nd	0.76	1.02
M15-23	12.096	2.205	0.0158	19	19.125	2.03	1.02	0.005	1.02	0.98
M15-24	7.647	1.210	0.2415	488	11.643	1.50	2.36	0.003	0.47	1.00
M15-26	8.529	1.363	0.2530	457	13.020	1.67	2.42	0.004	0.57	1.01
M18-01	6.334	0.898	0.098	25	9.197	1.23	3.44	nd	0.34	1.01
M18-02	7.299	0.403	0.0084	23	8.583	1.17	0.99	0.005	0.53	1.01
M18-05	6.895	0.462	0.0055	15	8.368	1.14	1.38	0.001	0.47	1.01
M18-07	6.767	0.449	0.0072	20	8.198	1.09	1.49	nd	0.46	0.99
M18-08	6.188	0.914	0.0097	25	9.102	1.21	3.23	nd	0.31	1.00
M18-09	6.173	0.923	0.0092	24	9.116	1.24	3.28	0.003	0.30	1.00
Sample L02										
M01-02	12.787	0.375	0.0095	17	13.982	0.19	0.52	0.009	2.84	1.01
M01-07	11.950	0.254	0.0101	16	12.760	0.18	0.45	0.005	2.59	1.00
M02-01	10.518	3.555	0.0172	19	21.853	2.59	3.72	nd	0.37	0.99
M02-02	10.226	3.643	0.0160	18	21.840	2.57	3.79	nd	0.39	1.00
M02-03	11.392	3.440	0.0156	17	22.36	2.73	3.88	nd	0.47	1.01
M02-04	8.440	3.412	0.0146	19	19.320	2.30	3.55	nd	0.26	1.02
M02-05	10.084	3.876	0.0155	17	22.440	2.60	3.93	nd	0.38	1.00
M02-06	9.319	3.531	0.0145	17	20.575	2.47	3.48	nd	0.32	1.02
M02-07	8.309	3.395	0.0122	16	19.132	2.34	3.60	nd	0.27	1.05
M02-08	9.299	3.260	0.0138	17	19.691	2.45	3.46	0.005	0.27	1.02
M02-09	9.117	3.515	0.0142	17	20.324	2.38	3.390	nd	0.31	1.00
M02-10	10.762	3.558	0.0169	19	22.104	2.66	3.89	nd	0.41	1.00
M02-11	10.876	3.538	0.0147	16	22.153	2.68	3.89	0.005	0.43	1.01
M02-12	9.080	4.037	0.0163	18	21.953	2.56	4.27	nd	0.28	1.02
M02-13	8.978	3.526	0.0148	18	20.218	2.36	3.49	nd	0.30	1.00
M05-01	9.011	4.367	0.0167	18	22.934	2.64	4.13	0.005	0.25	1.01
M05-02	8.925	4.060	0.0138	16	21.868	2.51	3.80	nd	0.26	1.00
M05-04	9.601	4.423	0.0162	17	23.702	2.71	4.06	nd	0.28	1.00
M05-05	8.249	4.227	0.0145	16	21.722	2.43	3.97	nd	0.23	1.00
M05-07	9.788	4.199	0.0176	19	23.174	2.71	3.86	nd	0.29	1.01
M05-09	9.164	4.085	0.0165	18	22.189	2.54	3.83	nd	0.30	1.01
M07-01	11.738	1.023	0.0111	17	14.999	0.52	0.59	0.011	2.32	0.99
M08-02	11.682	2.505	0.0137	16	19.667	0.58	1.40	0.018	2.58	0.99
M08-05	8.533	0.499	0.0095	22	10.123	0.40	0.87	0.012	1.61	0.98
M08-07	10.386	2.991	0.0119	14	19.920	0.38	4.45	0.010	2.67	1.01
M08-08	11.043	0.926	0.0123	20	13.995	0.36	1.13	0.007	2.35	1.00
M08-09	12.306	0.519	0.0121	20	13.959	0.26	0.65	0.009	2.67	1.00
Sample L05										
M02-01	5.986	1.244	0.0071	18	9.951	1.22	2.31	nd	0.35	1.01
M02-02	5.909	1.055	0.0059	16	9.273	1.15	2.36	0.002	0.32	0.98
M02-03	6.068	1.236	0.0071	17	10.007	1.22	2.36	nd	0.37	1.01
M02-04	6.055	1.061	0.0081	21	9.438	1.15	2.30	0.003	0.37	0.99

M02-05	6.196	1.101	0.0074	19	9.707	1.20	2.32	0.002	0.39	1.01
M02-06	5.807	1.362	0.0064	16	10.150	1.21	2.31	nd	0.32	1.00
M02-07	6.071	1.200	0.0071	18	9.895	1.21	2.33	nd	0.34	0.99
M02-08	6.068	1.132	0.0072	18	9.677	1.19	2.32	nd	0.35	0.99
M02-09	5.852	1.013	0.0064	17	9.080	1.11	2.36	0.003	0.38	1.00
M02-10	6.115	1.060	0.0076	20	9.495	1.15	2.31	0.005	0.44	1.03
M03-01	6.898	1.077	0.0051	12	10.330	1.47	2.32	nd	0.26	1.01
M03-02	6.865	1.093	0.0080	19	10.351	1.49	2.27	0.004	0.21	1.00
M03-03	6.661	0.463	0.0055	17	8.136	1.28	2.40	nd	0.24	1.00
M03-04	6.989	0.483	0.0067	19	8.530	1.34	2.53	nd	0.27	1.00
M03-05	7.015	0.511	0.0066	19	8.645	1.34	2.61	nd	0.29	1.01
M03-07	6.465	0.643	0.0067	19	8.963	1.27	2.31	nd	0.26	1.01

Notes: Age is apparent age for single spot. ThO_2 * is the sum of ThO_2 and the ThO_2 equivalent of UO_2. The standards used for analyze are described in the electoronic deposit document. nd = not detected.

TABLE 2. Representative electron microprobe analyses of ThO_2, UO_2, PbO, CaO, Y_2O_3 and S (wt.%) of xenotime grains in leucogranites, far-eastern Nepal

spots	ThO_2	UO_2	PbO_2	Age (Ma)	UO_2*	CaO	Y_2O_3	S
Sample L02								
X01-02	0.552	5.291	0.0153	21	5.464	0.277	39.1	0.017
X01-03	0.496	5.306	0.0113	15	5.461	0.305	38.7	0.018
X01-04	0.618	5.839	0.0189	23	6.033	0.273	38.5	0.016
X01-05	0.481	5.161	0.0091	12	5.312	0.276	38.3	0.014
X01-06	0.311	3.192	0.0094	21	3.290	0.209	38.4	0.009
X01-07	0.222	3.215	0.0092	21	3.285	0.216	38.1	0.005
X01-08	0.277	3.237	0.0081	18	3.324	0.197	38.7	0.010
X01-12	0.358	3.963	0.0086	15	4.075	0.226	38.5	0.018
X01-13	0.260	3.754	0.0086	16	3.835	0.246	39.2	0.009
X01-14	0.522	4.710	0.0134	20	4.874	0.313	37.7	0.011
X01-15	0.382	4.963	0.0127	18	5.083	0.290	37.2	0.011
X01-17	0.328	3.855	0.0099	18	3.958	0.231	36.8	0.011
X01-20	0.371	3.909	0.0097	18	4.025	0.214	38.4	0.016
X01-22	0.347	4.108	0.0129	23	4.217	0.239	38.4	0.013
X01-23	0.356	4.661	0.0097	15	4.773	0.296	37.7	0.016
X01-25	0.244	3.497	0.0092	19	3.573	0.247	38.3	0.011
X01-26	0.312	4.228	0.0136	23	4.325	0.255	38.1	0.015
X02-02	0.393	5.940	0.0151	18	6.063	0.337	36.6	0.011
X02-03	0.436	6.122	0.0194	23	6.259	0.345	35.6	0.011
X02-04	0.433	6.270	0.0155	18	6.406	0.354	35.5	0.013
X02-05	0.434	4.778	0.0105	16	4.914	0.369	36.1	0.008
X02-07	0.341	3.737	0.0105	17	3.844	0.231	38.3	0.009
X04-06	0.264	3.728	0.0087	20	3.811	0.261	37.40	0.009

Notes: Age is apparent age for single spot. UO_2* is the sum of UO_2 and the UO_2 equivalent of ThO_2.